TRIBHUVAN UNIVERSITY
INSTITUTE OF ENGINEERING
PULCHOWK CAMPUS

B-03-BAS-2020/2025

Design and Development of a Subsonic Wind Tunnel with a Gust Generator Featuring Oscillating Vanes

by
Aayush Khanal (077BAS001)
Anjana Thapa Magar (077BAS003)
Isha KC (077BAS012)
Ishan Kafle (077BAS013)
Nischal Raut (077BAS026)

A PROJECT REPORT SUBMITTED TO THE DEPARTMENT OF MECHANICAL AND AEROSPACE ENGINEERING IN PARTIAL FULFILLMENT OF THE REQUIREMENTS FOR THE DEGREE OF BACHELOR OF AEROSPACE ENGINEERING

DEPARTMENT OF MECHANICAL AND AEROSPACE ENGINEERING
LALITPUR, NEPAL

MARCH, 2025

COPYRIGHT

TRIBHUVAN UNIVERSITY

INSTITUTE OF ENGINEERING

PULCHOWK CAMPUS

DEPARTMENT OF MECHANICAL AND AEROSPACE ENGINEERING

The undersigned certify that they have read, and recommended to the Institute of Engineering for acceptance, a project report entitled **"Design and Development of a Subsonic Wind Tunnel with a Gust Generator Featuring Oscillating Vanes"** submitted by **Aayush Khanal, Anjana Thapa Magar, Isha KC, Ishan Kafle, Nischal Raut** in partial fulfillment of the requirements for the Bachelor's Degree in Aerospace Engineering.

Supervisor: **Asst. Prof. Kamal Darlami**
Department of Mechanical and Aerospace Engineering
Institute of Engineering, Pulchowk Campus

Supervisor: **Asst. Prof. Laxman Motra**
Department of Mechanical and Aerospace Engineering
Institute of Engineering, Pulchowk Campus

External Examiner: **Er. Salim Maharjan**
Visiting Faculty
Himalaya College of Engineering

Head of Department: **Asst. Prof. Dr. Sudip Bhattrai**
Department of Mechanical and Aerospace Engineering
Institute of Engineering, Pulchowk Campus

Date: March 9, 2025

ABSTRACT

Wind tunnels play a crucial role in aerodynamic experiments, facilitating the study of airflow behavior and its effects on various objects. They have several applications in the field of aerodynamics and fluid dynamics, one of which is the integration of a gust generator, which is crucial for studying gust effects on aerodynamic bodies. Without a gust generator, controlled gust conditions cannot be replicated, making it difficult to analyze their impact. This project focuses on the development of a subsonic wind tunnel with a contraction ratio of 6 and the design and integration of a gust generator into the wind tunnel capable of replicating a $1 - cosine$ longitudinal gust using oscillating vanes. Smoke visualization is performed to observe the generated gust. The analytical and simulation results are compared and show a good degree of agreement with an error of 10.63 %. The wind tunnel achieved a Turbulence Intensity (TI) of 0.88 % at the test section and 2.26 % at the outlet, with a calculated outlet error of 16.02 % with a mean velocity of 8.6 m/s. The vanes with optimal parameters of 25 cm chord, 4 Hz frequency, $15°$ deflection, and 300 mm spacing were used, yielding Re of 147186.21, St of 0.116 and k of 0.365 indicating unsteady flow. The wavelength of the generated gust of $4Hz$ has been calculated to be 208.437 cm with an error of 3.05 %. Hence, this study provides valuable insights into aerodynamic behavior induced by gust, contributing to the broader field of unsteady aerodynamics.

Keywords: *Wind Tunnel, Gust Generator, 1-Cosine Gust, Oscillating Airfoil, Flow Visualization*

ACKNOWLEDGMENTS

We extend our sincerest gratitude to our project supervisor, Asst. Prof. Kamal Darlami, Deputy Head of the Department of Mechanical and Aerospace Engineering, and Asst. Prof. Laxman Motra for their unwavering guidance, support, and inspiration throughout this project. Their invaluable supervision and insightful suggestions have made our journey much smoother than it would have been.

We express our heartfelt appreciation to the Department of Mechanical and Aerospace Engineering (DMAE), along with the Head of the Department, Dr. Sudip Bhattarai. We also acknowledge the Incubation Innovation and Entrepreneurship Center (IIEC) at the Institute of Engineering for providing us with the necessary workspace to conduct experimental work on wind tunnel construction, gust generation, and flow visualization analysis. We would also like to express our gratitude to the Carpentry Department for their invaluable assistance in building and assembling the wind tunnel. Their support and expertise were instrumental in the successful completion of this project.

In addition, we are deeply grateful to our seniors, teachers, and friends for their support during the various phases of the project. We remain open to constructive criticism and suggestions that may help improve the project. We deeply appreciate and value all the feedback that we have received.

Sincerely,
Aayush Khanal (077BAS001)
Anjana Thapa Magar (077BAS003)
Isha KC (077BAS012)
Ishan Kafle (077BAS013)
Nischal Raut (077BAS026)

TABLE OF CONTENTS

LIST OF FIGURES

LIST OF TABLES

LIST OF ABBREVIATIONS

AR Aspect Ratio

CFD Computational Fluid Dynamics

CFL Courant Friedrichs Lewy

CNC Computer numerical control

DMAE Department of Mechanical and Aerospace Engineering

EAS Equivalent Airspeed

ESC Electronic Speed Controller

GR Gust Ratio

IIEC Incubation Innovation and Entrepreneurship Center

LE Leading Edge

LED Light Emitting Diode

LEV Leading-Edge Vortex

MAV Micro Aerial Vehicle

PTV Particle Tracking Velocimetry

PVC Polyvinyl chloride

PWT Pulchowk Wind Tunnel

Re Reynolds Number

SST Shear Stress Transport

TI Turbulence Intensity

UAV Unmanned Aerial Vehicle

UDF User Defined Function

URANS Unsteady Reynolds-Averaged Navier-Stokes

CHAPTER ONE: INTRODUCTION

1.1. Background

1.1.1. Wind Tunnel

A wind tunnel is a structure used to study the aerodynamic properties of objects exposed to airflow under controlled conditions. It is a fundamental tool for experimental aerodynamics.

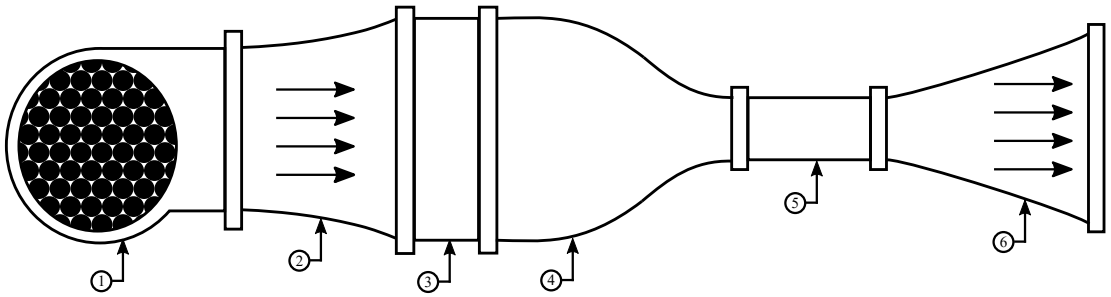

Figure 1.1: Schematic Diagram for Blower Wind Tunnel: (1) Blowing Fan; (2): First Diffuser; (3): Settling Chamber with Honeycombs; (4): Contraction Zone; (5): Test Section; (6): Second Diffuser

Figure 1.1 shows the schematic diagram of a subsonic, open-circuit, blower wind tunnel. A subsonic wind tunnel attains a maximum Mach number of 0.4. In a blower-type wind tunnel, the airflow is generated by a fan placed at the entrance that pushes the air into the wind tunnel. These tunnels are simpler to design and manufacture but can produce turbulence and noise. An open-circuit wind tunnels cost less for their construction and allow the use of a substantial quantity of visualization using smoke without the need to bleed. However, it is quite difficult to obtain a proper quality of the flow since they are subjected more to external disturbances and tend to be noisier [2].

Section (1) is the blowing fan, generally driven by an electric motor, which supplies the necessary pressure increase to counteract pressure losses in the tunnel circuit. Section (2) is the first diffuser, which slows down the airflow before the test section, reducing dynamic pressure. It helps to settle the turbulent airflow coming from the fans. Section (3) is the settling chamber, a large constant area section, where the flow is present at a low velocity and is, therefore, the ideal location for the placement of honeycombs and screens to make the flow regular. Section (4) is the contraction zone, which reduces in area continuously as defined by the contraction curve. In this section, the flow accelerates to its maximum velocity before entering the test section. Section (5) is the

test section, where the object to be tested is usually placed. It has the requirement of ease in accessibility and observability to facilitate the experimental procedure. The primary objective is to obtain a flow that is uniform and steady with minimal variation of velocity in the axial direction in this section. Section (6) is the second diffuser, which decelerates the flow efficiently to minimize kinetic energy losses. It is crucial to prevent flow separation in this section, as it can significantly diminish efficiency and adversely affect the overall performance of the wind tunnel.

Gusts are a critical phenomenon in the aerospace sector, whose effects are several and severe. For instance, the unsteady additional gust loads exerted on the structure can throw it right out of the flight envelope and act as the limiting factor. This leads to significant structural deformation and even failure if not accounted for properly in the design phase. Gust significantly adds to the static and fatigue loading conditions due to the increased bending moment on the root of the wing and leads to deformation of the wing [3]. It can change the aerodynamic characteristics of the aircraft abruptly, causing fluctuations in aerodynamic loads [4]. This results in decreased flight performance affecting stability and control [5]. Thus, it becomes necessary to understand the response of aircraft structures to gusts to be able to design the structures to withstand such effects and in essence to avoid the disastrous repercussions. Without a gust generator, controlled gust conditions cannot be replicated, making it difficult to analyze their impact. The most simple method to effectively produce gusts is to integrate the gust generator into the wind tunnel.

1.1.2. Gust

The flight of an aircraft is described in terms of the motion that is relative between the vehicle and the flow bounding it. Any phenomenon that tends to change this state of the flow will undoubtedly have an effect on it. Gust is such a phenomenon. A gust is defined as a sudden and brief increment in the magnitude of wind velocity as well as the direction compared to the average velocity of the wind in the region where the gust occurs. The magnitude of the gust is described in terms of its velocity, which needs to be considered such that it is compatible with aircraft dynamics. According to the regulations, a head-on gust is assumed to act at angles between $+\ 30°$and $-\ 30°$, assuming the most adverse conditions. From the sea level to altitudes up to $6096\ m$ $(20,000 ft)$ the velocity of the gust is taken to be $15.2\ m/s$ $(50\ fps)$ in Equivalent Airspeed (EAS). The magnitude linearly decreases to $7.6\ m/s$ $(25\ fps)$ in EAS up to $15240\ m$ $(50,000\ ft)$. The magnitude is assumed to be constant at any altitude above $50,000\ ft$. Overall, the velocity must build up in $2\ s$ at the most and last for $30\ s$ at the least [6].

1.1.3. Gust Characterization

Owing to its importance, gust modeling has received a particularly increasing interest in the research field over the years, the very first of which was published by NACA in 1915 [4]. This is necessary to categorize the gust for designing and certification purposes and is essentially achieved using a mathematical description of each type of gust. It is important to note that various subclasses of gust models exist; among these, only the ones currently adopted for designing and certification purposes are mentioned. These are simply categorized as discrete and continuous to maintain consistency with the current regulations [1].

1.1.3.1 Discrete Gust

It is a singular atmospheric flow structure that can manifest itself in different forms some of which are depicted in the Figure 1.2.a. In essence, transverse, streamwise, and vortex are the three types of discrete gust encounters [1]. All of these interact with the wing in their distinct ways to give unsteady variations in the effective angle of attack [4].

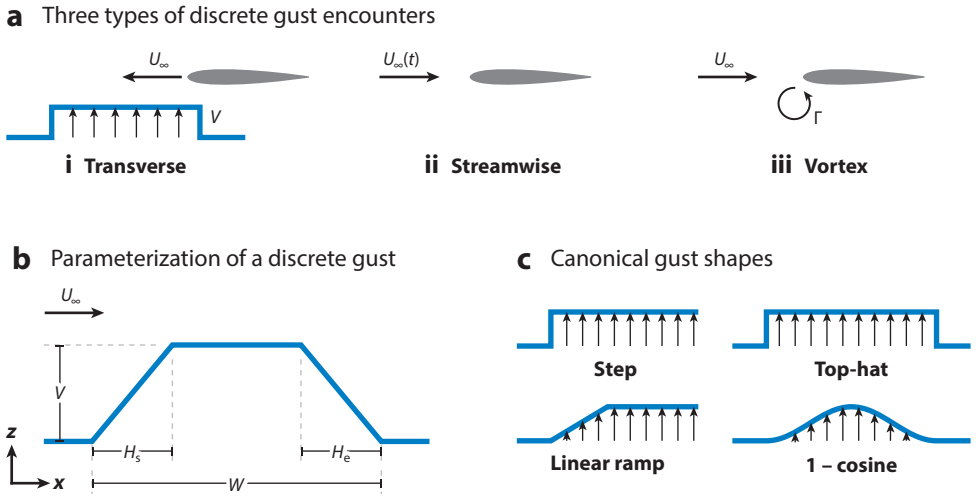

Figure 1.2: Characterization of Gust [1]

Transverse or normal gusts comprise velocities perpendicular to the lifting surface, that changes the flow angle. Streamwise gusts comprise velocities along the lifting surface. Unlike transverse gusts, they don't directly change the flow angle. In this scenario, changes in lift are due to variations in local dynamic pressure for small disturbances. However, for larger disturbances where flow separation occurs, viscous effects become significant. Vortex gusts are more complicated than transverse and streamwise gusts

because they create velocities in both directions. As a vortex gets closer to a wing, it inevitably interacts with it. When a vortex is sufficiently close to the wing's leading edge and boundary layer, it decays due to the pressure gradient (inviscid effects) and shear stress (viscous effects). In vortex–wing interactions, augmentation in the lift coefficient (C_L) occurs when the vortex gust impinges at the leading edge of the wing. This forms the counter-rotating Leading-Edge Vortex (LEV), followed by an opposite transient surge in C_L than usual upon reaching a distinct trailing edge before returning to normal [1].

Parameterization of discrete transverse gusts can be fundamentally achieved using their Gust Ratio (GR), velocity profile gradient distance (H), and width (W). H is the distance that gust requires to achieve its maximum velocity magnitude. The gust can be modeled either from one side or both sides, i.e., H signifies either or both H_s for arrival and H_e for exit. Figure 1.2.c represents the canonical profiles of velocity for discrete transverse gusts, which are dependent upon the value of H. The shapes shown are of step, top hat, ramp, and sinusoidal [1].

1. Sharp-edge gust:

   These include step and top-hat gusts, whose velocity profile is described by Equation 1.1 [4]. Here, V represents maximum gust velocity while $v(s)$ is the value of the velocity at the penetration distance ($s = U_\infty * t$).

$$\begin{aligned} \frac{v(s)}{V} &= 1 \quad (0 < s < H) \\ \frac{v(s)}{V} &= 0 \quad (s < 0 \quad or \quad s > H) \end{aligned} \tag{1.1}$$

2. Linear Ramp Gust:

   Their velocity have a linear increasing tendency with the gradient distance whose velocity profile is mathematically described by Equation 1.2 [4].

$$\begin{aligned} \frac{v(s)}{V} &= \frac{s}{H} \quad (0 < s < H) \\ \frac{v(s)}{V} &= 0 \quad (s < 0 \quad or \quad s > H) \end{aligned} \tag{1.2}$$

3. 1 - Cosine Gust:

   The current regulation seeks the replication of 1-cosine gust for all testing pur-

poses, whose shape is mathematically expressed by Equation 1.3 [4].

$$\begin{aligned} \frac{v(s)}{V} &= \frac{1}{2} * (1 - \cos(\frac{\pi s}{2H})) \quad (0 < s < 2H) \\ \frac{v(s)}{V} &= 0 \quad (s < 0 \quad or \quad s > 2H) \end{aligned} \tag{1.3}$$

1.1.3.2 Continuous Gust

Continuous gusts embody the atmospheric disturbances resulting in storms and clear air turbulence. This is done to better represent the continuous and random atmospheric gust conditions. This also accounts for the various gust frequencies that exist in the gusts and is therefore much more realistic than the discrete representation [1].

In actuality, gusts are a mixture of many flow structures including shear layers, coherent vortices, updrafts, downdrafts, and turbulence. During the conduct of the experiments, it is necessary to be driven by convenience and dissociate these various phenomena, pinpointing a specific phenomenon and highlighting its key effects [1].

1.1.4. Governing Equations

1.1.4.1 Theodorsen Model

The Theodorsen function, $C(k)$, is a complex-valued function representing the unsteady aerodynamic response of an airfoil. It is computed using the Hankel and Bessel functions:

$$C(k) = \frac{H_1^{(2)}(k)}{H_0^{(2)}(k) + iH_1^{(2)}(k)} \tag{1.4}$$

where $H_n^{(2)}(k)$ are the Hankel functions of the second kind.

This model is used to describe the unsteady aerodynamic forces on a body, particularly for airfoils undergoing oscillatory motion. The Theodorsen function takes into account the reduced frequency (κ), which is a measure of the oscillation rate relative to the flow velocity and describes both the reduction in amplitude and the phase change of the unsteady aerodynamic response that reflects how the oscillatory motion of the airfoil interacts with the surrounding flow, leading to time lags and reductions in the effective aerodynamic forces compared to a purely steady state [7, 8].

1.1.4.2 Bessel and Hankel Functions

Hankel functions are used to model propagating waves i.e., wake effects and lift-induced velocity in cylindrical geometry. The Hankel function gives the solution of Bessels equation. The Bessels equation is given as :

$$x^2\frac{d^2y}{dx^2} + x\frac{dy}{dx} + (x^2 - \nu^2)y = 0 \tag{1.5}$$

where:

- $y(x)$ is the unknown function,
- x is the independent variable, and
- ν is the order of the Bessel function.

It is a second order differential equation which governs oscillatory motions including airfoil oscillation to produce unsteady flow. The solution to Bessel's equation yields Bessels functions of the first and second kind which is given as follows:

$$y(x) = AJ_v(x) + BY_v(x) \tag{1.6}$$

where A and B are arbitrary constants, and v is the order of the function. $J_v(x)$ is the Bessel function of the first kind, which gives oscillatory solutions for finite values at $x = 0$, and $Y_v(x)$ is the Bessel function of the second kind, which diverges at $x = 0$.

The Hankel functions, or Bessel functions of the third kind, are combinations of Bessel functions and are written as:

$$H_n^{(1)}(x) = J_n(x) + iY_n(x) \tag{1.7}$$

$$H_n^{(2)}(x) = J_n(x) - iY_n(x) \tag{1.8}$$

The general solution can also be written as:

$$y(x) = AH_n^{(1)}(x) + BH_n^{(2)}(x) \tag{1.9}$$

where A and B are arbitrary constants.

Due to the linear independence of the Bessel function of the first and second kind, the Hankel functions provide an alternative pair of solutions to the Bessels differential equation [9]. $J_v(x)$ and $Y_v(x)$ are computed solving the following equations:

$$J_v(x) = \sum_{k=0}^{\infty} \frac{(-1)^k (x/2)^{\nu+2k}}{k!\Gamma(\nu+k+1)} = \frac{1}{\Gamma(1+\nu)} \left(\frac{x}{2}\right)^2 \left(1 - \frac{(\frac{x}{2})^2}{1(1+\nu)}\right) \tag{1.10}$$

$$Y_v(x) = \frac{J_v(x)cos(\nu\pi) - J_{-v}(x)}{sin(\nu\pi)} \tag{1.11}$$

1.1.4.3 Circulation

Circulation represents the total amount of rotation or vorticity around a closed contour, such as the path surrounding an airfoil. Mathematically, circulation (Γ) is defined as the line integral of the velocity field v around a closed curve C, as given by the following formula:

$$\Gamma = \oint_C \mathbf{v} \cdot d\mathbf{l} \tag{1.12}$$

Where:

- Γ is the circulation,
- $\mathbf{v}$ is the velocity vector at a point along the contour,
- $d\mathbf{l}$ is the infinitesimal line element along the contour.

The integral is taken around a closed curve (e.g., an airfoil). For an oscillating airfoil, or an airfoil experiencing unsteady motion, the circulation becomes dependent upon time.

In this case, the motion of the airfoil induces unsteady vortices in the flow field, which cause the circulation to vary over time [10]. The unsteady circulation can be written as:

$$\Gamma(t) = \Gamma_0 e^{i\omega t} \tag{1.13}$$

Where:

- $\Gamma(t)$ is the time-dependent circulation,
- Γ_0 is the constant amplitude of the circulation,
- ω is the angular frequency of the oscillation (in radians per second),
- t is time.

The circulation is given by the Kutta-Joukowski theorem and is calculated as:

$$\Gamma = 2\pi\alpha_0 U_\infty c C(k) e^{i\omega t} \tag{1.14}$$

where, α_0 is amplitude, U_∞ is free-stream velocity, c is chord, $C(k)$ is Theodorsen function, ω is angular velocity and t is time.

1.1.4.4 Biot-Savart Law

The Biot-Savart law is one of the most fundamental relations in the theory of inviscid, incompressible flow. It describes the velocity field induced by a distribution of vorticity in a fluid. A curved vortex filament induces a flow field in the surrounding space. If the circulation is taken about any path enclosing the filament, a constant value is obtained. Hence, the strength of the vortex filament is defined as Γ [10].

The radius vector from dl to an arbitrary point P in space is $\mathbf{r}$. The segment dl induces a velocity at P equal to:

$$\mathbf{v}(P) = \frac{\Gamma}{4\pi} \oint_C \frac{d\mathbf{l} \times \hat{\mathbf{r}}}{|\mathbf{r}|^2} \tag{1.15}$$

Where:

- $\mathbf{v}(P)$is the velocity at the point P induced by the vortex filament,
- Γ is the circulation (strength of the vortex filament),
- $d\mathbf{l}$ is an infinitesimal element along the vortex filament,
- $\hat{\mathbf{r}}$ is the unit vector pointing from the element $d\mathbf{l}$ to the point P,
- $|\mathbf{r}|$ is the distance from the element $d\mathbf{l}$ to the point P,
- The integral is taken along the closed contour C that encloses the vortex filament.

The vertical velocity induced by the oscillation of vanes is calculated as:

$$v = \text{Im}\left(\frac{-\Gamma}{2\pi z^2}\right) \tag{1.16}$$

where $z = x + iy$ is the complex coordinate of the point, and Γ is the time-dependent circulation.

1.1.4.5 Strouhal Number

The Strouhal number (St) is defined as:

$$St = \frac{fc}{U} \tag{1.17}$$

where f is the frequency, and c is the chord length and U is the velocity.

The Strouhal number indicates the relative significance of unsteady effects and helps quantify the gust. A low Strouhal number ($St < 0.1$) is common for large-scale flow oscillations. A moderate Strouhal number ($0.1 \leq St \leq 0.3$) is used to analyze unsteady flows due to pitching vanes. A high Strouhal number ($St > 0.3$) indicates heavy turbulence and extreme unsteadiness [11].

1.1.4.6 Reduced Frequency

The reduced frequency is defined as

$$k = \frac{\omega c}{2U} \tag{1.18}$$

where ω is the angular velocity , c is the chord length, and U is the velocity.

The reduced frequency is a dimensionless parameter that indicates the unsteadiness of the flow. A low reduced frequency ($k < 0.05$) represents quasi-steady flow conditions, where unsteady flow theories cannot be adopted. A high reduced frequency ($k > 0.05$) is used to analyze unsteady flows due to pitching vanes and indicates the presence of significant unsteady effects [12].

1.2. Problem Statement

The wind tunnel developed by Chaudhary [13] was initially designed to provide a uniform flow velocity of 12 m/s at the outlet. However, experimental measurements revealed that the maximum achievable velocity was around 5 m/s. The flow was highly non-uniform at the outlet of the wind tunnel. Consequently, a new wind tunnel was required, maintaining uniform flow conditions for accurate gust generation. The simplest method of generating gusts is to integrate the gust generator inside the wind tunnel. The study of gust generation is important for various aerodynamic applications, particularly for understanding controlled unsteady flow behavior.

Gusts play a crucial role in aerodynamic studies, influencing various aspects of flow dynamics. Controlled gust generation enables researchers to study unsteady flow phenomena, improve experimental validation of numerical simulations, and develop techniques to mitigate unsteady aerodynamic effects. However, without a gust generator, replicating controlled gust conditions remains a challenge, limiting the ability to analyze their impact on flow structures.

With the advent of Computational Fluid Dynamics (CFD), the task of simulating such phenomena has become comparatively simplified. Yet, experimental validation remains essential, especially for characterizing gust-induced flow fields under controlled conditions. The lack of reliable experimental data on gust formation and propagation necessitates the development of a dedicated setup for gust generation. This project aims to tackle two critical problems: design a wind tunnel that ensures a uniform airflow of 10 m/s at the outlet and integrate an active gust generator capable of producing controlled gusts, enabling better understanding and modeling of unsteady aerodynamic behavior.

1.3. Objective

1.3.1. Main Objective

To design and fabricate a low-speed wind tunnel with an integrated gust generator capable of experimentally observing the 1-cosine gust profile.

1.3.2. Specific Objectives

i. To design and develop a low-speed wind tunnel for obtaining uniform flow of 10 m/s at the outlet.

ii. To design and fabricate a gust generator using oscillating vanes for producing a sinusoidal longitudinal gust.

iii. To set up a smoke visualization system to observe and analyze the generated gust profile.

iv. To compare the analytical and simulation results and qualitatively validate the generated gust profile.

1.4. Scope of Work

As the current project focuses on designing, fabricating, and testing a low-speed wind tunnel integrated with a gust generator, it can be used to study the sinusoidal gust effects. The wind tunnel is designed to maintain a uniform $10\ m/s$ flow, ensuring accurate gust visualization. This project provides a foundation for further research on gust mitigation techniques, real-time gust adaptation techniques, and advanced aerodynamic testing for Unmanned Aerial Vehicle (UAV) and other aerial vehicles.

1.5. Applications

The possible applications of the project are listed below:

i. Wind tunnels can be used to study the airflow properties of objects such as lift, drag and moment.

ii. Wind tunnels can be utilized for studying large-scale aerial vehicles, provided that the *Reynolds Number (Re)* is maintained. This ensures that insights gained from small-scale experiments remain applicable to full-scale studies.

iii. The effect of gusts on UAV and other aerial vehicles can be studied, which is crucial for their design, given by regulations.

iv. Gust can essentially be a troublesome phenomenon for aircrafts. This explains the rigorous research being undergone for the development of active and passive gust load alleviation strategies on a multitude of aerodynamic models. However, due to the novel and early experiential nature of these models, a wind tunnel based gust system allows for convenient, safe and speedy progress rather than the risky outdoors.

v. Structural deformation of the part that is exposed to the flow as a result of gust loading can also be measured using the gust generator system.

vi. The sudden increase in the angle of attack due to the encountered gusts can result in flow separation. This can be studied using the gust generator system with the help of visualization techniques.

vii. It is also possible to study the effects of gusts on buildings, bridges, radio towers, power lines, wind turbines and so on using a gust generator system.

viii. The study of aero-elasticity using the gust system is also achievable, a topic which has received considerable attention from researchers and experimentalists alike.

1.6. System Requirements

The system used in our project is divided into software and hardware as shown in Table 1.1 and 1.2 .

1.6.1. Hardware Requirements

The list of hardware that was used in our project are shown below:

Table 1.1: Hardware Categorization

Category	**Item**
Electronics and Actuation	12V Power Supply
	Aluminum Flexible Shaft Coupling (4 mm × 8 mm)
	Aluminum Spar (12 mm)
	Arduino Uno R3
	Bearings
	Jumper Wires
	Lathe Machine
	Motor Driver (TB6600)
	Stepper Motor
Experiment	High Processing Computer
	Vane Anemometer
	Wind Tunnel
Fabrication	Metal Pipe (2.54 cm)
	3D Printing Filament
	AC Welder
	Carpentry Tools
	CNC Laser Cutting Machine
	Marble Cutter
	Plywood
	Smoothing Tape
	Styrofoam
	Wooden Beams
Flow Visualization	3-cell Lithium-ion Battery (11.2 V)
	Duct Fan
	Iphone 14 Pro Max
	Pixel 8a
	Plane Laser
	PVC Pipes (2.54 cm)
	Servo Tester
	Smoke Collector
	Smoke Generator

1.6.2. Software Requirements

The list of software that was used in our project are shown below:

Table 1.2: Software Categorization

Category	**Item**
Designing	CATIA *V5*
	SOLIDWORKS *v2023*
Simulation and Data Processing	ANSYS FLUENT *v2022*
	Fidelity Pointwise *v2023*
	ImageJ
	Inkscape
	MATLAB *v2023*
	Tecplot 360 *v2024*
Electronics	Arduino IDE
Documentation	MS Excel *v2024*
	TeXstudio

CHAPTER TWO: LITERATURE REVIEW

2.1. Wind Tunnel

Low subsonic wind tunnels have served as a powerful medium to provide a large amount of data in experimental aerodynamics. This is crucial because of the growing applications of UAV, Micro Aerial Vehicle (MAV), and wind turbines that have directed the focus towards low Re aerodynamic experiments [14]. Therefore, numerous studies on the design and construction of subsonic wind tunnels exist, some of which have been referenced in this report and summarized in this section.

The length of the test section is defined in terms of the hydraulic diameter. Barlow et. al. provides a relationship between the hydraulic diameter and the cross-section of the test section [15], as shown below:

$$D_h = 2\sqrt{\frac{\Omega_{TS}}{\pi}} \tag{2.19}$$

Here D_h is the hydraulic diameter and Ω_{TS} is the cross-section of the test section.

For the test section length, $(0.5 - 3)D_h$ is considered an acceptable range to avoid boundary layer separation at the test section and ensure uniform airflow. If the length is less than $0.5D_h$, then it would be difficult to obtain uniform flow. If the length is more than $3D_h$, then the boundary layer would be likely to increase in thickness. Mauro et. al. selected a value of 2 as a good trade-off to avoid the two extremes [16]. According to Mehta et. al., a common rule of thumb for the sizing of the test section is to have a rectangular section with a ratio of 1.4 - 1 [17]. To facilitate the observation of visualization techniques such as smoke, it is possible to construct the test section with access doors or walls made of acrylic. The test section can also be illuminated with Light Emitting Diode (LED) lamps [18].

The contraction section can be considered to be the most essential part of the wind tunnel that determines the flow velocity as well as uniformity in the test section and has to be designed very carefully. It is also the section that is the most difficult to design.

The study performed by Bell et. al. highlights the influence of contraction geometry on boundary layer behavior, noting that 3D effects become significant in lower Aspect Ratio (AR). Different contraction shapes of walls were evaluated to minimize boundary layer separation and to obtain uniform flow. The profiles selected for the study are

third-order polynomial, fifth-order polynomial, seventh-order polynomial and matched cubics. Computational tests confirmed that the fifth-order polynomial shape was the most effective in preventing separation and also maintaining a reasonable Re and flow uniformity. The study of various length-to-height ratios (L / H) was also conducted. Neglecting excessively short and long contraction lengths is necessary as it leads to separation at the inlet and exit due to adverse pressure gradients [19].

The contraction area ratio is a very important parameter that has to be picked with proper consideration since it affects the entire efficiency of the wind tunnel. A large area ratio results in a higher flow acceleration and lower total pressure losses at the end of the section. Conversely, a very low area ratio causes high pressure losses in the upstream wind tunnel components. A very high area ratio results in wind tunnel with excessively large dimensions. Bell et. al. concluded that the area ratio in the range of 6-10 is optimal to avoid the adverse effects. The nozzle cross-section area ratio should be in the range of 6 – 10 [19]. Using an area ratio less than 6 leads to high pressure losses in the upstream wind tunnel components, while an area ratio higher than 10 results in an excessive inlet cross-section dimensions. Mauro et. al. used an area ratio of 7 as it provides a good trade-off between performance and dimensions. In an open-loop wind tunnel, the cross-section of the settling chamber is equal to the components that come before and after it: contraction curve and inlet. The cross-section of the chamber is constant [16]. Generally, the length of the section is taken to be 0.5 times the diameter of the inlet [20].

It is common for a combination of honeycombs and screens to be placed in the test section. The cells of the honeycomb should be aligned with the direction of the flow to reduce fluctuations in the transverse velocity. In the stream wise direction, it's effects are minimal, as it leads to a very small reduction in the pressure.

The major design factors to be considered are porosity, which is the ratio between actual flow cross-sectional area and total cross-sectional area; hydraulic diameter, which characterizes the effective diameter of a non-circular conduit for fluid flow analysis; and length. From the geometric dimensions of the honeycomb, parameters such as the number of divisions, cell lengths, and cross sectional areas are determined. A complementary parameter to porosity is solidity, which is the ratio between cross-sectional area of the solid sheet and the total cross-sectional area. Hence, the relation between them is as shown below [16].

$$\sigma_h + \beta_h = 1 \tag{2.20}$$

Here σ_h is the solidity and is β_h the porosity. This relation allows the calculation of porosity. The cell hydraulic diameter is calculated using the equality of areas. The study conducted by Loehrke et. al. concluded that shorter cells (5-10 cell diameters) are adequate for turbulence control [21].

Introducing a fine screen ahead of the honeycomb reduces streamwise turbulence. Farell et. al. concluded that using a combination of honeycombs and screens results in greater turbulence reduction than using honeycomb alone [22]. Work conducted by Prandtl showed that using multiple screens with varying mesh sizes is more effective in reducing turbulence than using a single screen.

An important design parameter is the porosity of the screen, which should ideally in the range of 0.58 - 0.8 [16]. Another important parameter is the spacing between the screens. Two properties need to be considered. Firstly, the flow should fully recover from the perturbation caused by the first screen before reaching the next. This allows the pressure drops in the screens to remain independent from each other. Secondly, the minimum spacing should be of the order of the larger of the eddies generated by the screen. A spacing of 0 - 2 times the cross-section diameter of the test section is found to be an ideal value. A very small spacing causes the flow to become highly distorted after the last screen while a very large spacing causes high boundary layer growth [17].

2.2. Gust Generator

Gust can be generated using various means. Gust generator systems can be classified into two categories. One of them is the passive method, where we bring some form of blockage into a flow that will interact to produce turbulence. Another method involves the active type, which utilizes controllable moving vanes or tabs that disseminate the flow into larger flow structures and lend it the turbulent energy required to simulate the required gust condition [23].

An active method for gust generation is chosen for the production of a 1-cosine discrete gust as per the regulation FAR 14 CFR Part 25 [6]. It helps to maximize the gust velocity and also allows for the adjustment of the gust frequency. An oscillating-vane gust generator was chosen due to its ability to produce large longitudinal and lateral gusts, simplicity of implementation, and suitability for the test section size [23]. These

types of gust generators have been successfully used to produce large wind gusts in a variety of wind tunnels [12, 24, 25, 26]. Oscillating vanes are simply airfoils that span the entire width or height of the wind tunnel and rotate in an oscillatory motion to produce a change in the pitch. This is similar to forcing a change in the angle of attack of the flow simulating the atmospheric gust condition and has been integrated in the wind tunnel by Lancelot et. al. [12].

2.2.1. Vanes

The vanes can be placed vertically or horizontally in the wind tunnel as per convenience, although placing the vanes vertically is preferred over horizontal placement to avoid gravity effects [27]. The vane airfoil needs to be thick due to lower airspeed and rotate rapidly. Both static and dynamic loads need to be considered during the structural design process. Static load tests check how the vane holds up under constant pressure, while dynamic load tests see how it copes with changing forces. The vanes need to be extended through the entire wall of the wind tunnel to prevent any wingtip vortices and limit the size of the computational domain. The vane material selection should be done carefully. Some essential criteria to be considered are the material weight, machinability, toughness, stiffness, and smoothness [12]. Styrofoam is a reasonable material because it provides a balance among the several properties mentioned. An aluminum spar is added on the quarter-chord point of the vane for the actuation purpose. It was surface-impregnated with epoxy resin to increase its toughness and smoothness [12].

Regarding the number of vanes, having only one gust vane penalizes the uniformity of the gust formed in space. This leads to the formation of a wake especially directly behind the gust generator. Increasing the number of vanes can be considered to improve gust uniformity. However, crowding the vanes too close together due to the improper designation of numbers and lack of available space results in undesirable interaction between the flow wake and the model while increasing the complexity of fabrication and setup. Setting up two vanes is a good compromise between gust uniformity and fabrication, and setup complexity [28]. Using a smaller chord will lead to a more lightweight structure in contrast with thicker chords. Lower rotational inertia and reduced aerodynamic loads act on them, thereby decreasing the power requirements. However, the amplitude of the gust will be lower. On the other hand, a greater chord will increase the gust amplitude but this will need to be compensated with increased structural strength and actuation power requirements [24].

Considering that the two vanes are placed with a small vertical separation, the amplitude of the gust can be increased. However, we need to account for the non-uniformity in the gust, produced due to the smaller useful working area between the two vane wakes. On the other hand, increasing the spacing will have the opposite effect, complementing the required gust uniformity but with lower gust amplitude [24]. The minimum allowable separation between the vanes should be the summation of the chord length of the vanes, while the maximum separation should be less than the space of tangent of the curve at the contraction zone [26].

2.2.2. Actuation System

Over the years, development of gust generator have been done using cam-based, servo motors, and stepper motors. A cam-based system, for instance, is a simple and cost-effective solution that employs rotational motion to produce linear displacement; however, it suffers from limitations in fine-tuning the intensity and frequency components in the gust profiles generated, resulting in an unsteady airflow profile [25]. Servo motors also have been frequently used for gust generators. They offer closed-loop control of both position and speed, allowing adjustable intensity and frequency of gust profiles. Servo motors are normally configured with a gear head between the motor and the gust vanes, reducing power and torque requirements but offering precision location. Lancelot et. al. describes how their servo system, controlled in a feedback loop, ensures accurate vane movement with smooth, high-frequency updates ($1\ kHz$), allowing for precise gust simulation [12]. Despite the accuracy of the system, it may face some issues at high intensity gust generators [12, 29]. Stepper motors are also used in gust generator system because of their programmability and control over frequencies of oscillation. French et. al. describes the use of a hybrid stepper motor which produces enough torque ($12.75\ N-m$) for the intended gust generator designs. Although stepper motors may not be the ideal choice for generating high-frequency gusts, they can generate repeatable and controlled gust profiles [23].

CHAPTER THREE: METHODOLOGY

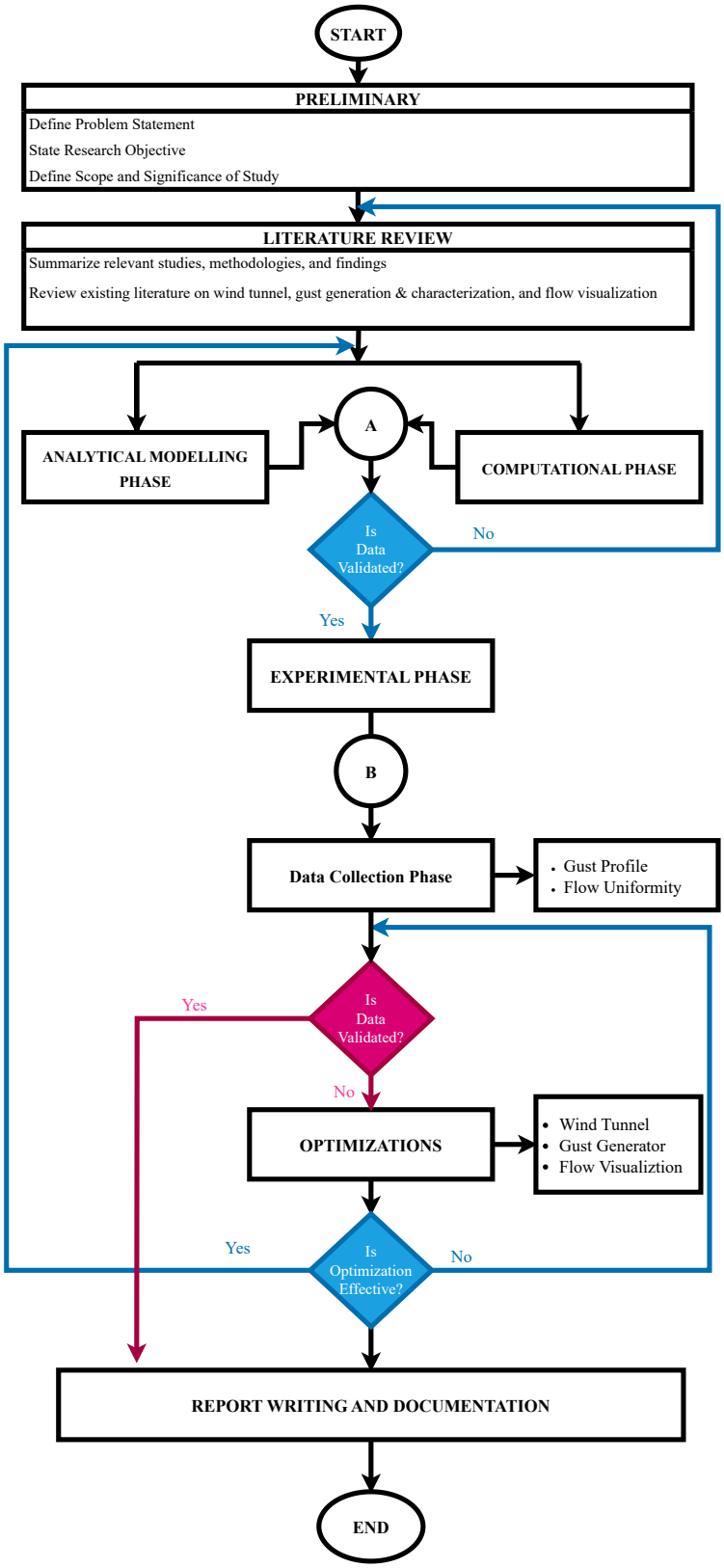

Figure 3.3: Methodology Flowchart

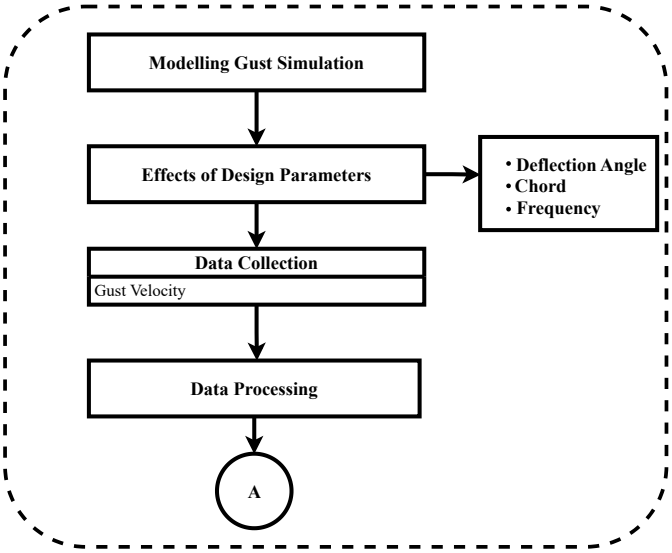

Figure 3.4: Analytical Modeling Phase Flowchart

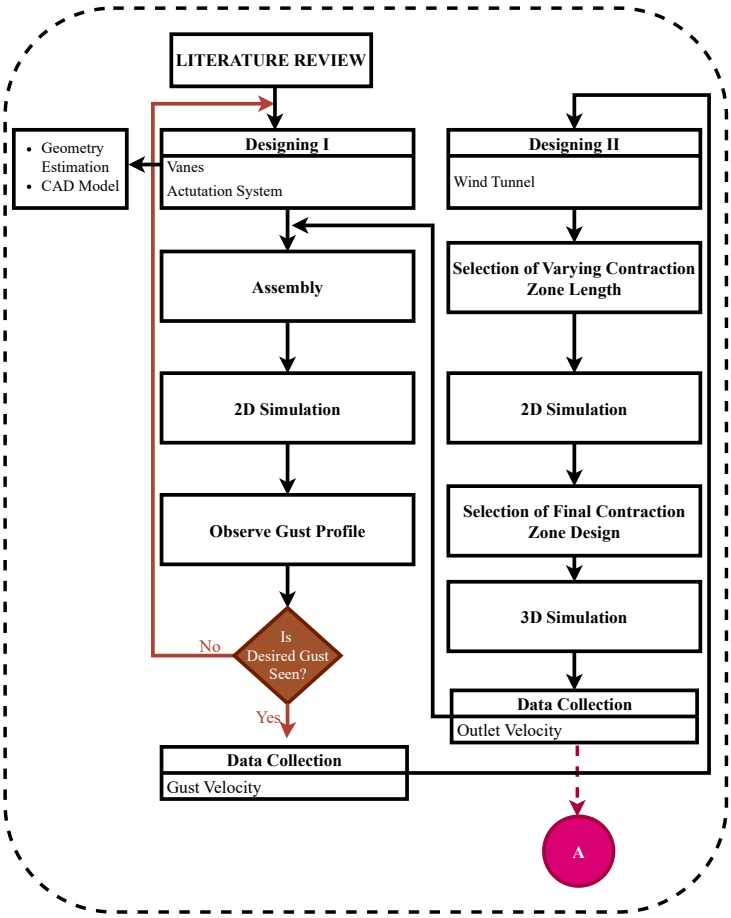

Figure 3.5: Computational Phase Flowchart

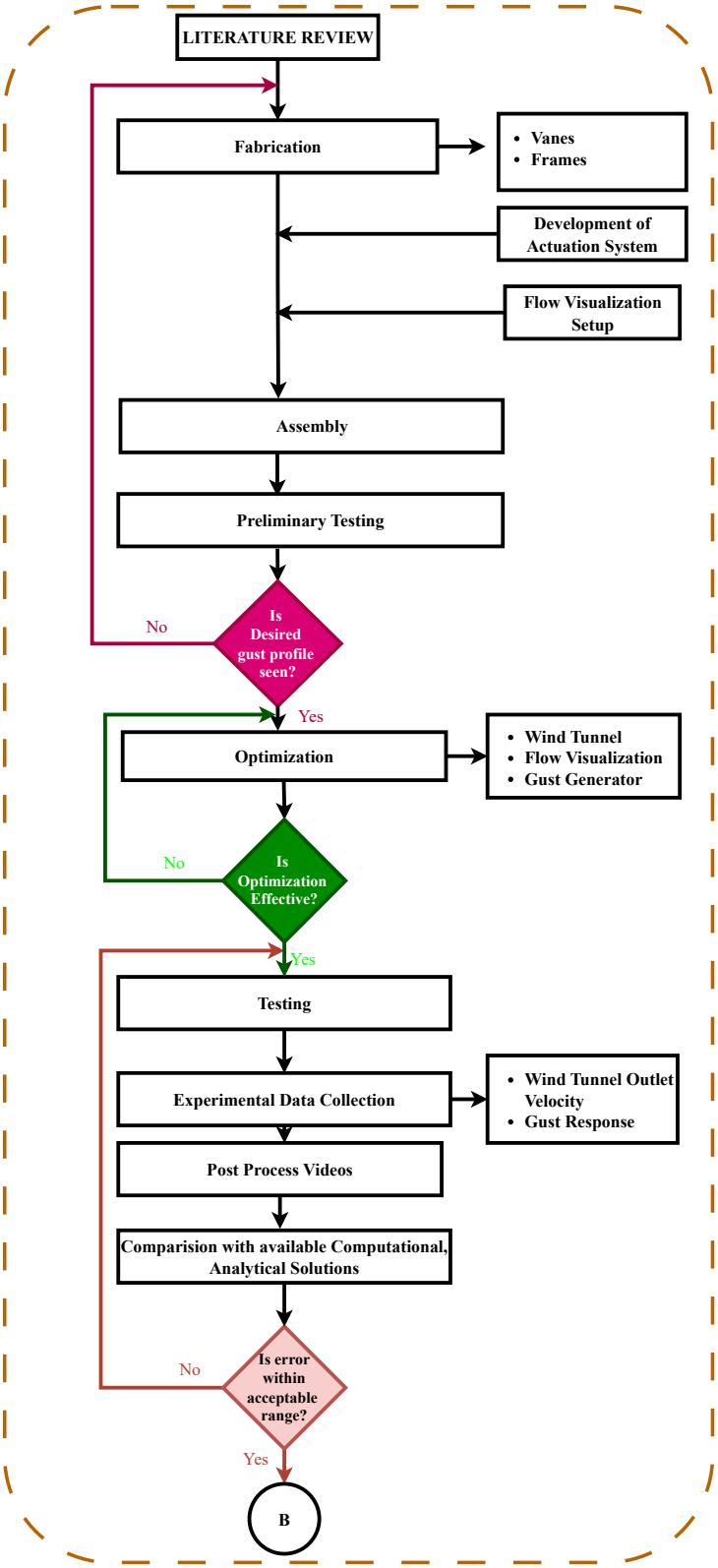

Figure 3.6: Experimental Phase Flowchart

3.1. Preliminary Phase

In this phase, initial research was conducted to establish a clear understanding of the project's objectives and significance. The scope was outlined, and a well-defined problem statement was formulated to guide the study.

3.2. Computational Phase

At this stage, various findings on the effects of airfoils undergoing upstroke and down stroke motion were analyzed. A comprehensive review of gust generator fabrication over the years was conducted which included how the gust vanes were designed and how they were actuated. Additionally, a study on the design of wind tunnel was carried out. These insights were ultimately incorporated into our project.

3.3. Numerical Methodology

Before proceeding with the phases outlined in Figure 3.3, simulation i.e., computational phase was conducted. This was crucial for understanding the gust characteristics under varying parameters and for determining an optimal set of conditions for experimental observations.The computational phase have followed the steps outlined in Figure 3.5.

3.3.1. Governing Equations

The incompressible Unsteady Reynolds-Averaged Navier-Stokes (URANS) governing equations were employed, as given in Equation 3.21 and 3.22, to simulate the unsteady phenomena i.e., pitching up and down motion of the airfoil [30] .

Equation of Continuity:

$$\nabla \cdot u = 0 \tag{3.21}$$

Equation of Momentum:

$$\rho \left(\frac{\partial \vec{u}}{\partial t} + \vec{u} \cdot \nabla \vec{u} \right) = -\nabla p + \nabla \cdot \tau_{ij} + \vec{f} \tag{3.22}$$

where the viscous shear stress tensor τ_{ij} is given as:

$$\tau_{ij} = \tau_{ij}^{L} + \tau_{ij}^{T} \tag{3.23}$$

$$\tau^L = \mu\left(\nabla\vec{u} + (\nabla\vec{u})^T\right) - \frac{2}{3}\mu(\nabla\cdot\vec{u})I \tag{3.24}$$

The k - ω Shear Stress Transport (SST) turbulence model was selected, as no significant differences in the results obtained from the convergence of Courant Friedrichs Lewy (CFL) at 1, as reported by YIGILI et. al. [31]. Also, k - ω SST showed better performance in enclosed flows compared to k - ϵ SST [26].

$$CFL = \frac{U\Delta t}{\Delta x} \tag{3.25}$$

The instantaneous angle of attack, α, defining the oscillating motion of an airfoil, was varied sinusoidally according to Equation 3.26.

$$\alpha(t) = \alpha_0 + \alpha_a sin(\omega t) \tag{3.26}$$

where, α is the angle of attack that varies with time, α_0 is the mean angle of attack, α_a is the amplitude, ω is the frequency in radians per second, and t is the time in seconds.

3.3.2. Computational Model and Mesh

The Pulchowk Campus wind tunnel, developed by Chaudhary, is a subsonic open-circuit wind tunnel [13]. The gust vanes were pivoted at the quarter chord location ($0.25\ c$) from Leading Edge (LE) of the airfoil. A rectangular grid for 2 vane configuration was used as shown in Figure 3.7, for which ANSYS FLUENT solver was used to simulate the dynamic motion. The mesh was created using Fidelity Pointwise, that allowed meshing process a lot smoother than in-built ANSYS meshing software.

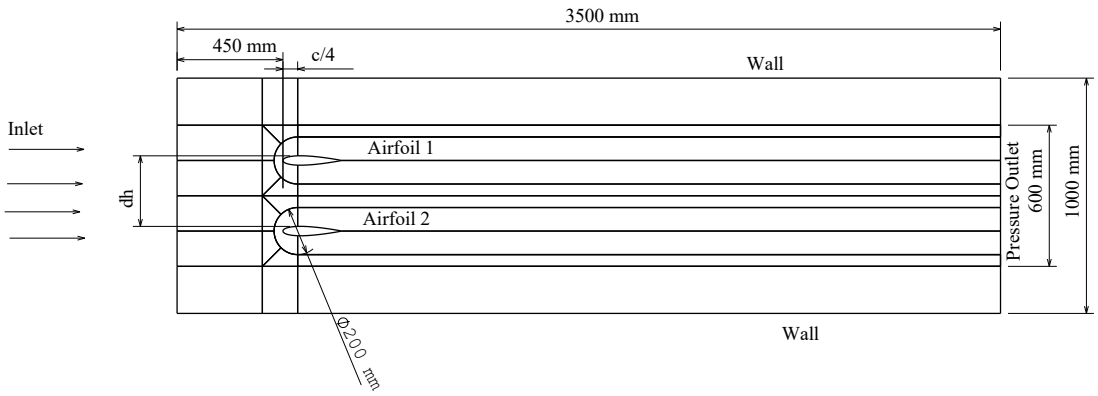

Figure 3.7: Simulation Domain Discretization

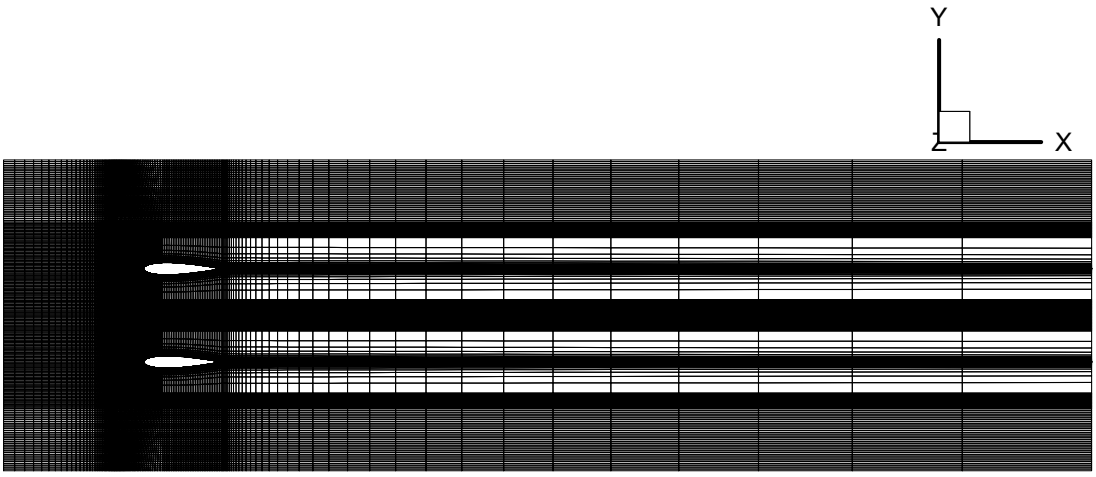

Figure 3.8: Coarse Mesh Domain for 25 cm chord

Grid Independence tests as reported in YIGILI et. al., showed no significant change in the induced vertical velocity so this test was postponed to the optimization phase [31]. A structured rectangular grid of $1000\,m \times 3500\,m$ was used for the simulation as shown in Figure 3.7. The grid was applied with a growth rate of 1.2 for 25 layers near LE and the spacing were made constant for a $y+$ of 0.5. The grid configuration near the airfoil is shown as Figure 3.9.

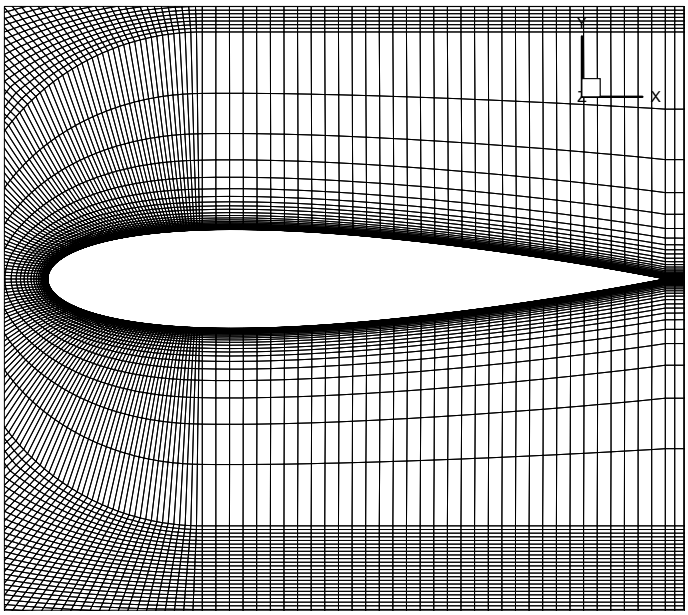

Figure 3.9: Near Airfoil Mesh

The design parameters that needed to be studied were varied to study its effects as shown in Table 3.3. These included the spacing between them (dh), chord length (c),

frequency (f), and maximum deflection angle (θ_{max}).

Table 3.3: Parameters for Studying Effects

Design Parameter	Values
Spacing between gust vanes (dh)	$1c$, $1.5c$, $2c$
Chord Length (c)	$20, 25, 30$ (cm)
Frequency (f)	$2, 3, 4$ (Hz)
Maximum deflection angle (θ_{max})	$5°$, $10°$, $15°$

In ANSYS Fluent, dynamic meshing was performed by compiling the User Defined Function (UDF) file, provided in Listing 1. The mesh was configured with a diffusion parameter of 1.5, and smoothing and re-meshing were applied. These dynamic mesh regions governed the simple harmonic motion.

3.3.3. Boundary Conditions

The streamwise velocity was specified at the inlet, while the outlet was set as pressure outlet with zero gauge pressure. No-slip and adiabatic conditions were applied to the airfoils and walls, as these walls represent the tunnel boundaries. The density and viscosity were assumed constants at $1.2\ kgm^{-3}$ at $293\ K$, and 1.812×10^{-5}, respectively.

Table 3.4: Boundary Conditions for Simulation

Flow Parameter	**Value**	**Flow Parameter**	**Value**
Velocity (U_∞)	$5ms^{-1}$	Reynolds Number	82742.59
Chord Length (c)	$20, 25, 30\ cm$	Reduced Frequency	0.314
Temperature	$293K$	Pitching Amplitude	$10°$
Density	$1.2kgm^{-3}$	Pitching Axis	$0.25c$
Dynamic Viscosity	$1.812851\times10^{-5}N \cdot s \cdot m^{-2}$	Time Step Size	$0.002s$
Total Time Step	1000		

3.3.4. Modeling of the Vanes

The vanes for this study were modeled using CATIA V5 software. The available styrofoam material at the department was not sufficiently thick to consider thicker airfoil profiles. As a result, NACA 0016, was selected for modeling the vanes. The total height of each vane is $720\ mm$ and the model of designed frame is shown in Figure C.1.

3.4. Analytical Modeling Phase

In this section, the vertical velocity induced by two oscillating airfoils was analytically solved given by Equation 1.16 to demonstrate the generation of a sinusoidal gust downstream. Using the unsteady aerodynamic Theodorsen model and the Biot-Savart law, the induced vertical velocity at a designated observation point was computed.

The total velocity at the observation point was taken as the superposition of contributions from both the airfoils. A phase correction was also introduced to align the simulated and analytical results, reducing the phase mismatch and improving agreement with the result from simulation.

The solution was obtained by varying the following parameters:

Table 3.5: Varying Parameters

Parameter	**Values**
Chord Length (cm)	$20, 25, 30$
Amplitude ($\theta°$)	$5, 10, 15$
Frequency (Hz)	$2, 3, 4$

Plots of vertical velocity versus time were obtained in MATLAB at ($x = 1\ m$, $y = 0\ m$).

3.5. Experimental Phase

3.5.1. Vane and Frame Fabrication

After selecting the vane configuration from the simulation phase, the vanes were manufactured using a Computer numerical control (CNC) Foam Cutter and Styrofoam. The surfaces were sanded to smoothen, and smoothing tape was wrapped around the vanes to improve their toughness as shown in Figure C.8. A hole with a diameter of $10\ mm$ at quarter-chord was placed to provide the pitching axis. An aluminum solid rod was inserted into this hole, which was then integrated into the initially designed frame, manufactured with corresponding holes based on results from the simulation as shown in Figure C.9.

3.5.2. Actuation System

For the actuation purpose, stepper motors were selected, specifically Nema-23, capable of providing $1.89\ Nm$ holding Torque. They were driven via TB6600 motor driver with the help of Arduino Uno. The Arduino was programmed to deliver the correct step sequence to the motor driver. The schematic diagram for the electronic circuit required is shown in Figure 3.10. In order to join the stepper motor with the spar, an aluminum flexible shaft coupling was used for the connection.

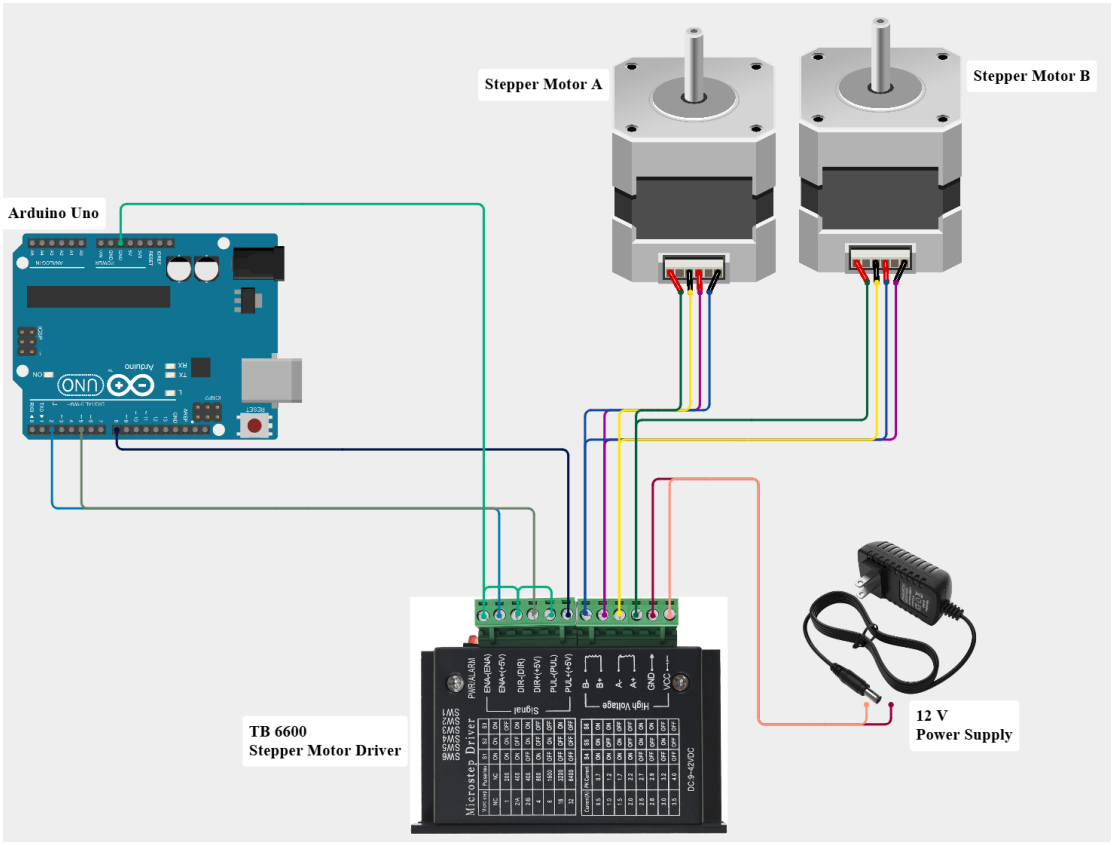

Figure 3.10: Schematic Diagram for Actuation Circuit

Micro stepping was enabled from TB6600 to *6400 revolutions per cycle* to reduce the vibration produced from the motors. The number of steps, delay for the motor to replicate the frequency was done using Table 3.6. It was found that the delay for the actuation is $0.02\ sec$ from expected value.

Table 3.6: Stepper Motor Input Parameters

Parameter	**Value 1**	**Value 2**
Frequency	$2\ Hz$	-
Time for Half Oscillation	$0.125\ s$	-
One Complete Oscillation	6400 steps	$360°$
Desired Degree of Oscillation	177.778 steps	$10°$
Time for One Step	$7.03 \times 10^{-4}\ s$	-
Delay	$703.125\ \mu s$	-

3.5.3. Preliminary Testing

Experimental observations were then conducted to visualize the gust generated using smoke. The parameters were selected based on the results obtained from simulation. Two vanes, each with a chord length $25\ cm$, were positioned at $1.5\ c$ distance apart. The vanes were oscillated at a frequency of $2\ Hz$ with a maximum deflection angle of $10°$.

During oscillation, the vanes were held in position by the designed frame as shown in Figure C.9. The frame was installed into the wind tunnel test section outlet. Actuation was performed using stepper motors. Smoke was injected through a series of pipes connected to the smoke generator outlet.

3.6. Data Collection

The output observed was the gust profile and the uniformity of the wind tunnel flow at the outlet.

3.7. Optimization

The optimization procedure adopted is explained in this section.

3.7.1. Design of Wind Tunnel

The wind tunnel was designed using CATIA. The main factors considered in the design process were a uniform flow of velocity of $10\ m/s$ at wind tunnel outlet. The design of the entire wind tunnel is based on these considerations.

The Pulchowk wind tunnel designed by Chaudhary inlet consists of an array of ten

blower fans present as the drive system of the wind tunnel [13]. The dimension of the inlet section is $2.95\ m \times 1.15\ m$, which was determined on the basis of the fan diameter of $20\ in$. To accommodate the fans in the matrix of 5×2 while avoiding interference, a width of $116\ in$ and a height of $45\ in$ was necessary. The inlet features ten evenly spaced holes with a diameter of $20.5\ in$ to facilitate the airflow into the wind tunnel. The inlet was left unaltered for the designing and manufacturing purposes. The details of the fan is provided in the Table B.7.

The simulations were conducted from the region where a consistent velocity of $1.5\ m/s$ was observed, which occurred at the end of the previous wind tunnel's settling chamber at $0.85\ m$. The dimensions of this section are the same as those of inlet, i.e., $2.95\ m \times 1.15\ m$. A length of $450\ mm$ was chosen for the settling chamber based on the simulation performed, which confirmed that the velocity contour at the test section was adequately uniform.

The contraction profile was obtained using a fifth-degree polynomial curve, given by Equation 3.27, to achieve flow uniformity and prevent boundary layer separation. MATLAB software was used to apply the following equation to obtain the profile.

$$Y(X) = H_i - (H_i - H_e)[6(X')^5 - 15(X')^4 + 10(X')^3] \tag{3.27}$$

The theoretical contraction ratio of the entire wind tunnel was set to 6. However, considering that the space for the test section was not much narrower, the width of the tunnel was selected as $0.52\ m$, and the height was $1\ m$. In actuality, the contraction ratio was determined as follows:

$$\begin{aligned} \text{Actual Contraction Ratio} = \frac{\text{Inlet Area}}{\text{Outlet Area}} = \frac{2.95 \times 1.15}{0.52 \times 1} = \frac{3.3925}{0.52} \\ = 6.524 \end{aligned} \tag{3.28}$$

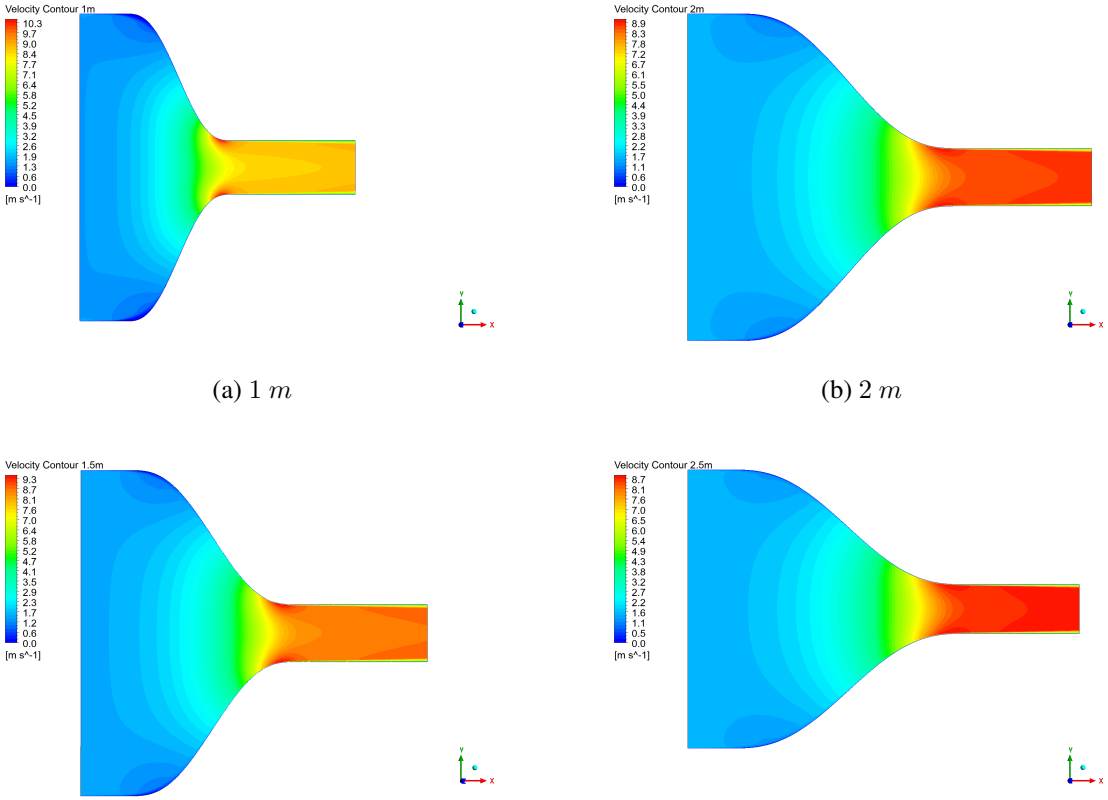

(a) 1 m (b) 2 m

(c) 1.5 m (d) 2.5 m

Figure 3.11: Velocity Contour for Different Contraction Zone Length

The length of the contraction section was varied between 1000 mm, 1500 mm, 2000 mm and 2500 mm. 2D simulations were performed using ANSYS FLUENT and velocity magnitude contours were analyzed as shown in Figure 3.11. The results showed that the flow accelerated most uniformly for a contraction length of 2500 mm. Hence, a contraction length of 2500 mm was selected for the contraction section. A 3D model was then designed for this length as shown in Figure 3.12 and simulations were performed, confirming its suitability.

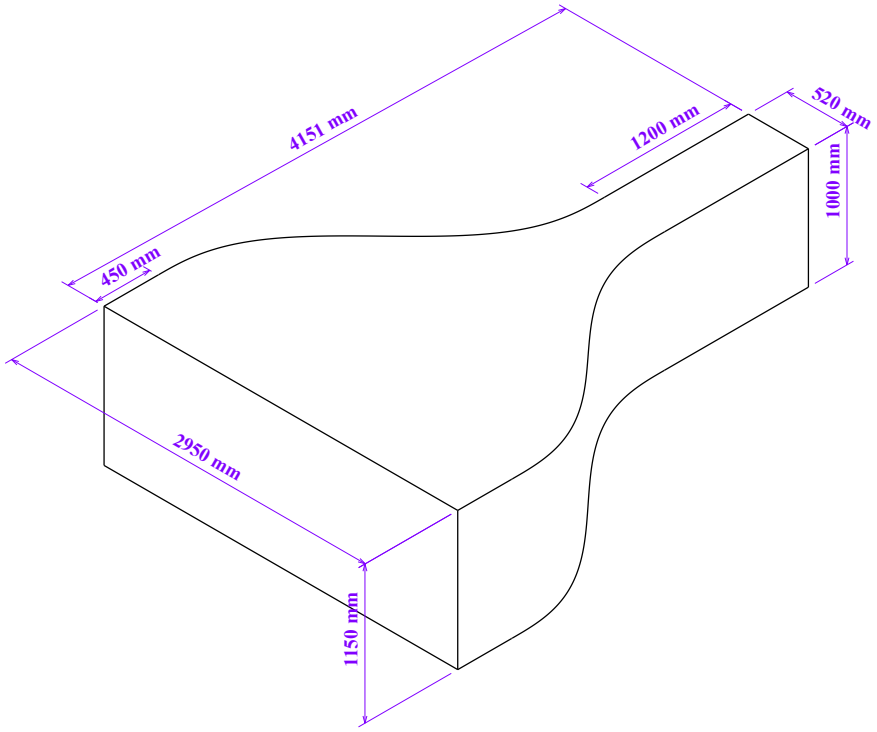

Figure 3.12: New Wind Tunnel Section

The designed wind tunnel has a hydraulic length of $1\ m$, and the minimum required diffuser length for static pressure recovery is five times the hydraulic length, making the total tunnel length $10\ m$. However, due to space and resource constraints, the diffuser section was omitted from the design.

Grid Independence for the wind tunnel was done evaluating the averaged velocity at the outlet section at different mesh sizes. The edges were refined with a factor of $\sqrt{2}$, growth rate of 1.2 for 25 layers both at the beginning and ending of the edges. 3D simulation was performed with the inlet velocity set to $1.5\ m/s$ and with a TI of $40\ \%$, obtained using Equation 3.29. The maximum and minimum velocity recorded was 3.3 m/s and $1.4\ m/s$ at the inlet of new wind tunnel design.

Table 3.7: Grid Independence Study Size

Mesh Type	Mesh Size
Coarse	853,200
Medium	2,434,825
Fine	6,868,800

The total length of the wind tunnel was obtained to be $5\ m$. The overall dimensions of the individual sections of the wind tunnel are presented in Table 3.8, which are labeled further in Figure 3.13.

Table 3.8: Wind Tunnel Dimensions

Section	Dimension
Inlet	$2.95\ m\ (W) \times 1.15\ m\ (H)$
Settling Chamber	$2.95\ m\ (W) \times 1.15\ m\ (H) \times 1.3\ m\ (L)$
Contraction Zone	$2.5\ m\ (L)$
Test Section	$0.52\ m\ (W) \times 1\ m\ (H) \times 1.2\ m\ (L)$

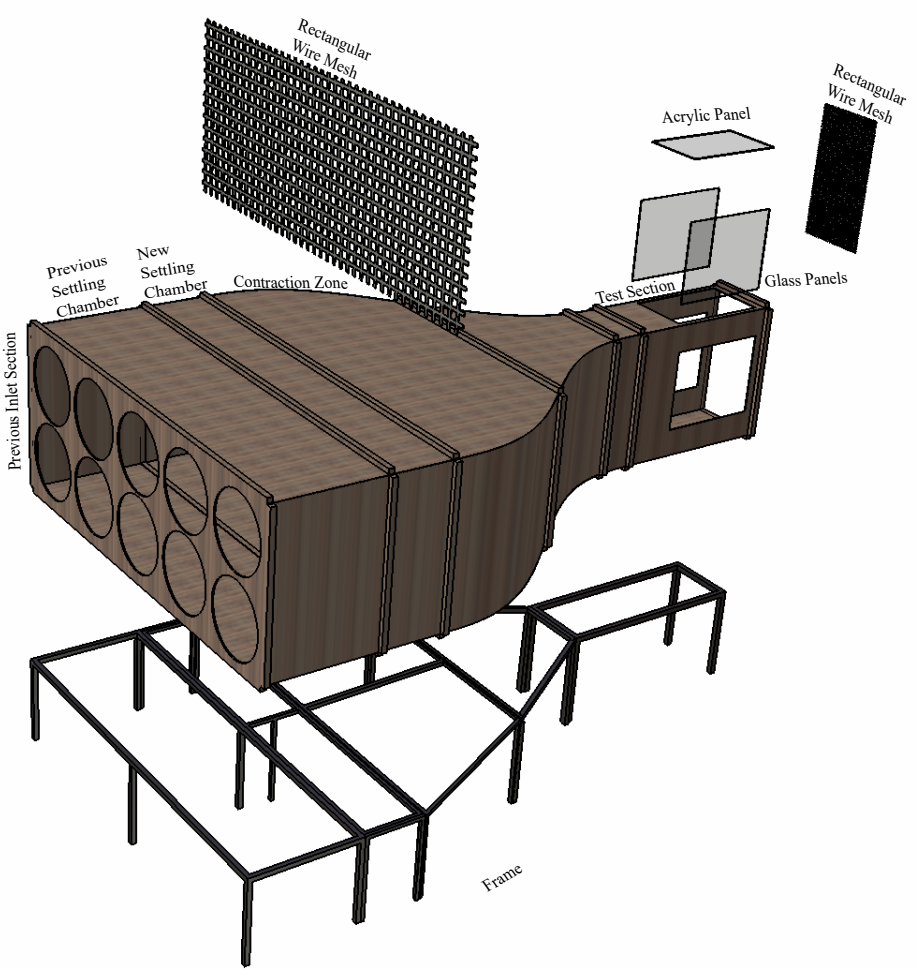

Figure 3.13: Wind Tunnel Parts Labeled

3.7.2. Fabrication of Wind Tunnel

The designed wind tunnel was manufactured at IIEC. The remaining sections for the tunnel were individually fabricated, assembled, and attached to the main inlet section to

develop an open-circuit fan array (blower-type) subsonic wind tunnel. The frame, which serves as the support structure to hold the wind tunnel, was designed and fabricated using $2.54 \times 2.54\ cm^2$ metallic square pipes. The base frame to support the wind tunnel was also designed as shown in Figure 3.14.

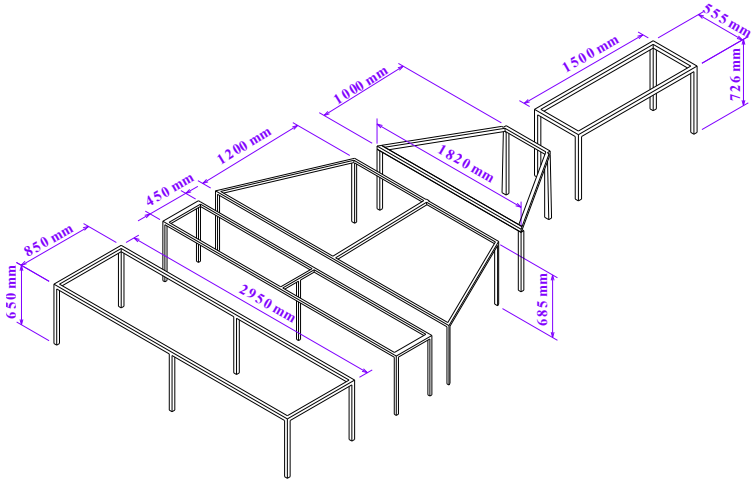

Figure 3.14: Wind Tunnel Base Frame

The entire length of the tunnel was divided into four sections to provide ease during cutting and assembly. Optimal areas of the designed wind tunnel sections to be cut were marked using CATIA Drafting module as shown in Figure C.7. The required plywood was procured, and the necessary portions and curvatures were marked and cut using a CNC laser cutter available at the Manufacturing Lab of DMAE. A plywood thickness of $3\ mm$ was used for the top and bottom sections, while a $5\ mm$ flexible plywood was used for the contraction section. The contraction zone was fabricated using the trapezoidal approximation, i.e., marking the inlet and outlet heights, and nails were hammered to hold the sides with wooden beams. Assistance from the Pulchowk Carpentry department was sought during the assembling of the wind tunnel. The sections were connected to each other with M10 bolts.

At the test section, a hinged door was installed to provide access for the model to be placed inside. For ease of observation, a rectangular transparent glass panel of $0.5\ m \times 0.5\ m$ was embedded in the side wall of the section. Additionally, a rectangular acrylic sheet of $1\ m\ (L) \times 0.5\ m\ (W)$ was placed on the top surface. The interior of the test section was painted black to enhance smoke visualization. Two rectangular wire meshes were added in the settling chamber to reduce the large eddy vortices. Any gaps resulting from imperfections in the joining process were filled by attaching Formica

plywood of $0.8\ m$ at the joining edges. The final assembled wind tunnel is shown in Figure 3.15.

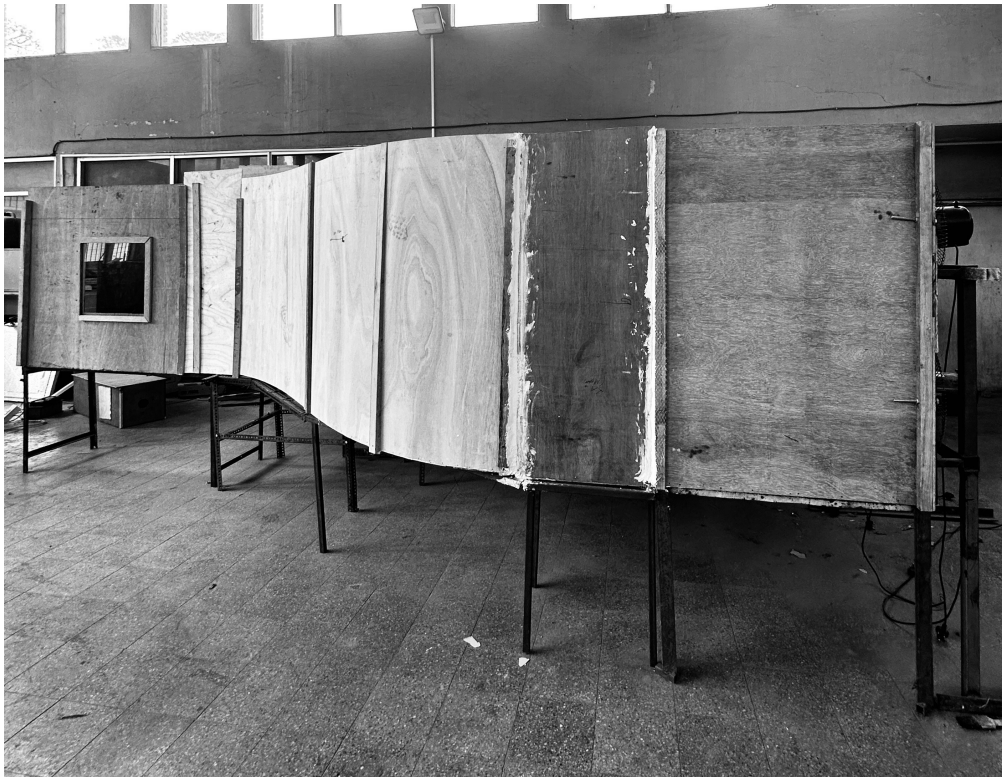

Figure 3.15: Side View of Manufactured Wind Tunnel

The gust profile can be properly visualized after the flow is fully developed. The test section was not sufficient to develop the flow. Hence, a detachable test section of $1.8\ m$ as shown in Figure C.13 was fabricated with glass panels and was assembled.

3.7.3. Smoke Generation Mechanism

To enhance smoke intensity, the smoke generation mechanism was also optimized. The outlet of the smoke generator is connected to a reservoir equipped with a valve, allowing momentary accumulation of smoke before release. A duct fan, powered by a three-cell lithium ion battery and regulated via a combination of Electronic Speed Controller (ESC) and a Servo tester, was placed at the outlet of the reservoir to facilitate suction of the collected smoke, which is directed outwards into the flow through a series of Polyvinyl chloride (PVC) pipes. The schematic diagram for the setup is as shown in Figure 3.16. The smoke has been injected at $400\ mm$ from the beginning of test section and $30\ mm$ downwards from upper wall.

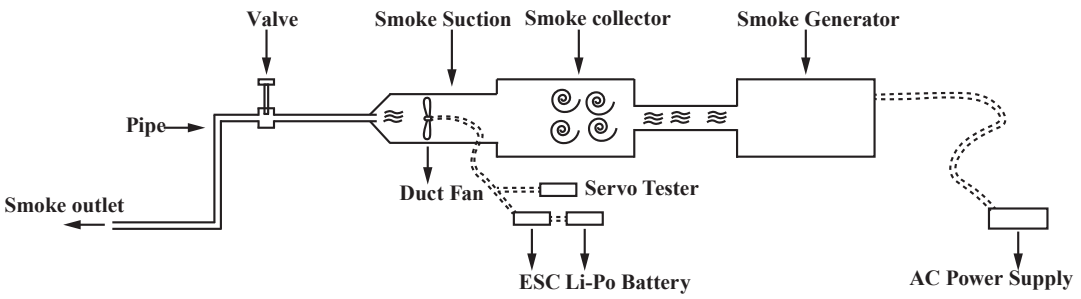

Figure 3.16: Schematic Diagram of Smoke Generation Mechanism

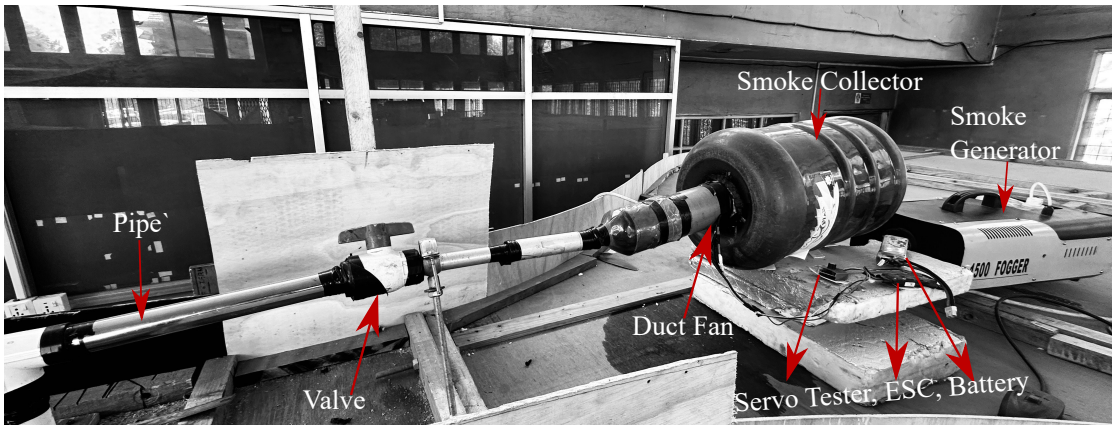

Figure 3.17: Experimental Smoke Generation System

3.7.4. Actuation System

Clamps were 3D-printed to secure the stepper motors, preventing unintended rotation that was seen in 1^{st} phase of the experiment and minimize vibrations. The dimensions for the clamp is shown in Figure C.5. An Aluminum Flexible Shaft Coupling of ($4\ mm \times 8\ mm$) was installed between the motors and the spars. The spars were drilled on a lathe machine to ensure proper transmission of rotary motion from stepper motors. The spars were integrated with the vanes into the wind tunnel at desired spacing. The upper ends of the spars were supported by bearings housed within 3D-printed casings, whose dimension is as shown in Figure C.6. The overall setup for the optimized actuation system is shown in Figure 3.18 and 3.19. The weight was added to counter the unexpected movement of base frame.

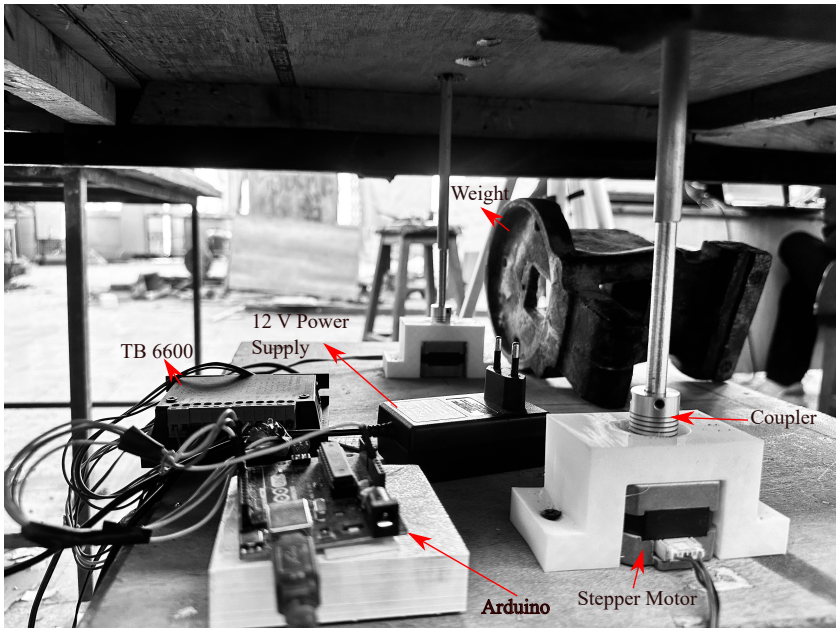

Figure 3.18: Actuation Experimental Setup (Base)

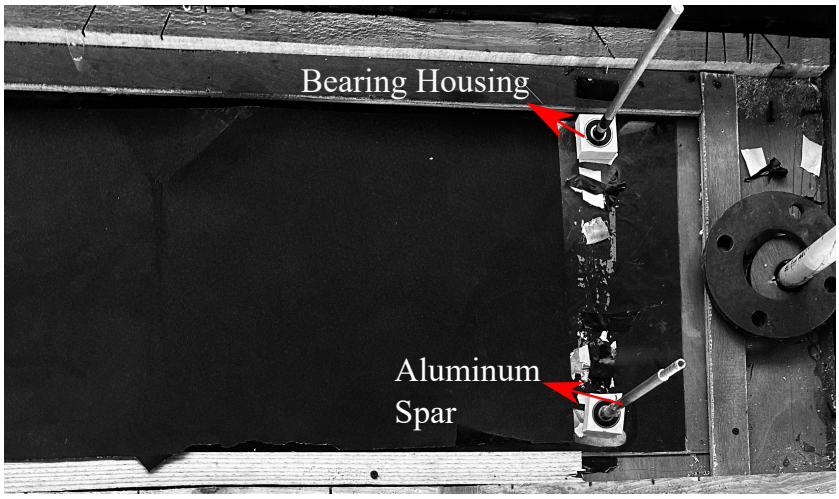

Figure 3.19: Actuation Experimental Setup (Top)

3.7.5. Computational Phase II

Simulations were carried out again after obtaining a set of optimal parameters from experiment with updated parameters shown in Table 3.9. The parameters were selected as two vanes with chord length of $250\ mm$ spaced $300\ mm$ apart and oscillating with a frequency of $4\ Hz$ with a deflection angle of $15°$. The inlet velocity was set to $8.6\ m/s$ with a TI of $0.88\ \%$. All other parameters were kept the same and the induced vertical velocity obtained at a point $(x = 1000\ mm\ ,\ y = 0\ mm)$.

Table 3.9: Updated Parameters for Simulation

Parameter	**Value**
Inlet Velocity(m/s)	8.6
Turbulence Intensity (TI %)	0.88
Reynolds Number	147186.21
Reduced Frequency	0.365

The mesh was now refined with a refinement factor of $\sqrt{2}$. The grid independence was done by computing the vertical induced velocity at ($x = 1000\ mm$, $y = 0\ mm$) with coarse, medium, and fine meshes.

Table 3.10: Grid Independence Study for Gust Simulation

Label	**Number of Elements**
Coarse	51,475
Medium	130,105
Fine	216,859

Simulations were also performed for $20\ cm$ chord vanes varying their separation between $1c$, $1.5c$, and $2c$. The vanes were oscillated at $2\ Hz$ with a deflection angle of $10°$. This was done to study the effect of spacing on gust profile, as this effect was not studied in the previous phase.

3.7.6. Analytical Modeling Phase II

Analytical modeling was repeated with the free stream velocity set to $8.6\ m/s$. The parameters were selected as two vanes with chord length of $25\ cm$ spaced $300\ mm$ apart and oscillating with a frequency of $4\ Hz$ with a deflection angle of $15°$. All other parameters remained unchanged. The induced vertical velocity was measured at ($x = 1\ m$, $y = 0\ m$).

3.7.7. Experimental Phase II

Testing includes evaluating the uniformity and velocity of the wind tunnel outlet and test section flow. Uniformity was assessed by measuring and calculating the turbulence intensity at the outlet and test section. A 10 x 5 grid with $10\ cm$ x $10\ cm$ cells was created using thread as shown in Figure 3.21. At the center of each grid cell, three sets of maximum and minimum velocity measurements were taken using a vane anemometer

available at the DMAE. The recorded data were then averaged. The averaged values were used to calculate the turbulence intensity using the Equation 3.29.

$$\text{TI } \% = \frac{U'}{U_{mean}} \times 100 \tag{3.29}$$

Where,

- U' represents the difference between the maximum velocity (U_{max}) and mean velocity (U_{mean}).
- U_{mean} is the average between the maximum (U_{max}) and minimum (U_{min}) velocities.

Experimental observations were then reconducted to analyze the gust generated. The schematic diagram illustrating the complete experimental setup is shown in Figure 3.20.

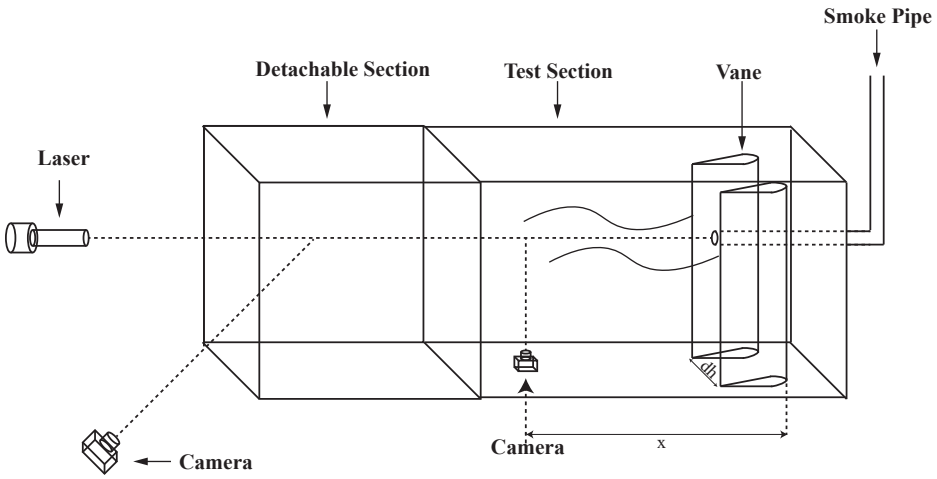

Figure 3.20: Schematic Diagram of the Experimental Setup (*Dimension in mm dh: 200, 300 mm, x: 1000 mm*)

Three sets of vanes of chord lengths 20, 25 and 30 cm were fabricated. The parameters were varied for the different chord lengths as; frequency (2, 3, 4 Hz), Deflection angle (5°, 10°, 15°), and vane spacing (200, 300, 400 mm). The vanes were oscillated while being secured in position using the new frame as shown in Figure 3.23 and actuation setup. Due to the stepper motors heating up, each experiment was conducted only for a duration of around 30 s at a time. The smoke was introduced into the flow using the

smoke generation mechanism. Smoke, combined with a plane laser as shown in Figure 3.22 was used for visualization of the gust.

Figure 3.21: Division of the Wind Tunnel Outlet

Figure 3.22: Plane Laser Projection at the Outlet of Smoke Pipe

Figure 3.23: Integration of Vanes in the Wind Tunnel

3.7.8. Data Collection Phase II

The data collected was maximum and minimum flow velocity at wind tunnel outlet and test section. Also the visualized gust profiles remarks were recorded in the logbook as shown in Appendix D. The wavelength of the generated gust was measured.

3.8. Documentation

All the procedures conducted throughout the project have been documented along with the results. This information has been reported concisely in the standard format indicating the successful completion of the project. Finally, conclusions have been drawn, shortcomings and possible future enhancements have been listed as well.

CHAPTER FOUR: RESULTS AND DISCUSSIONS

4.1. Analytical & Simulation Result Before Optimization

The upstroke, midstroke, and downstroke of the gust vanes are shown in Figures 4.24, 4.25, and 4.26, respectively. These figures indicate the generation of 1-cosine gust profile. Also, the upstroke phase leads to an increase in the velocity within the domain.

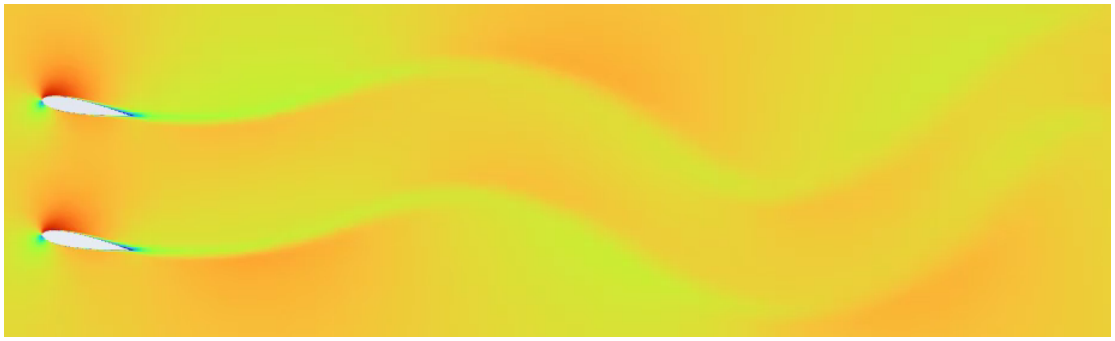

Figure 4.24: Deflection of Two Vanes Upstroke

Figure 4.25: Deflection of Two Vanes MidStroke

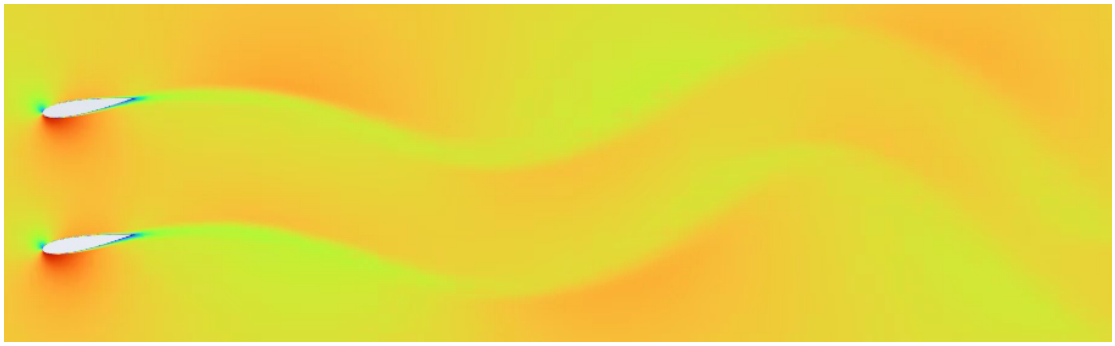

Figure 4.26: Deflection of Two Vanes Downstroke

The effects of other design parameters shown in Table 3.3 for the two vanes configuration are studied further below.

4.1.1. Effect of Varying Deflection Angle

An increase in gust velocity is observed with the increment in the deflection angle, which in turn increases the vertical induced velocity. Minimum error is observed at a deflection angle of $\theta_{max} = 10°$. This confirms $10°$ is enough to produce a uniform gust profile.

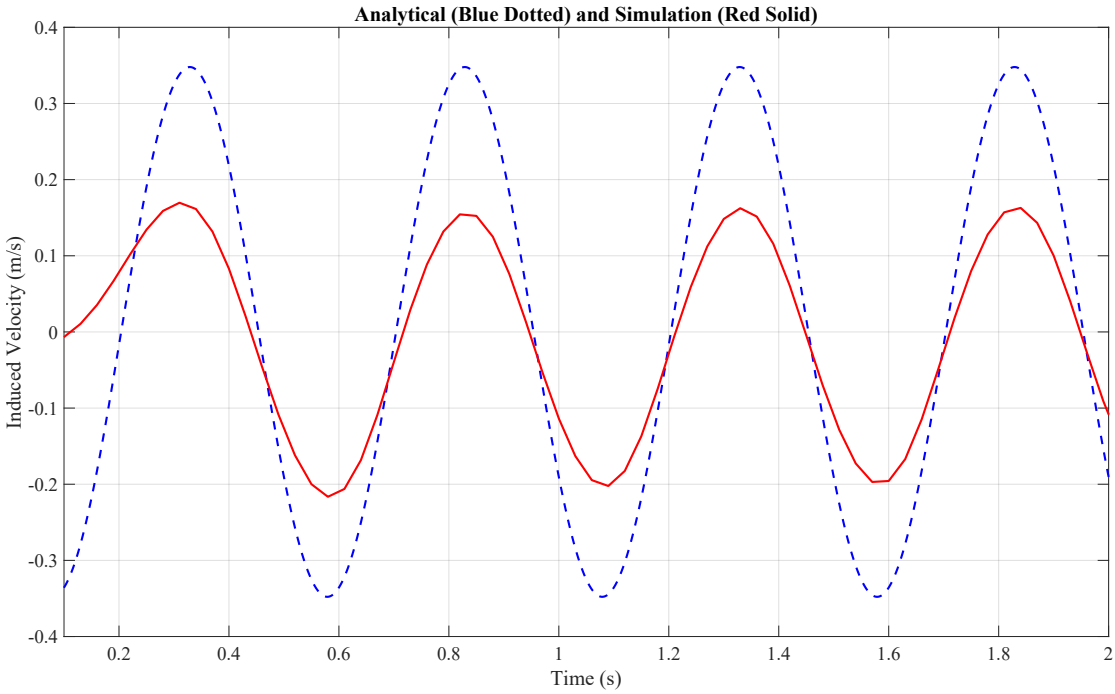

Figure 4.27: Vertical Velocity versus Time for $c = 0.25m$, $f = 2Hz$, $\theta_{max} = 5°$

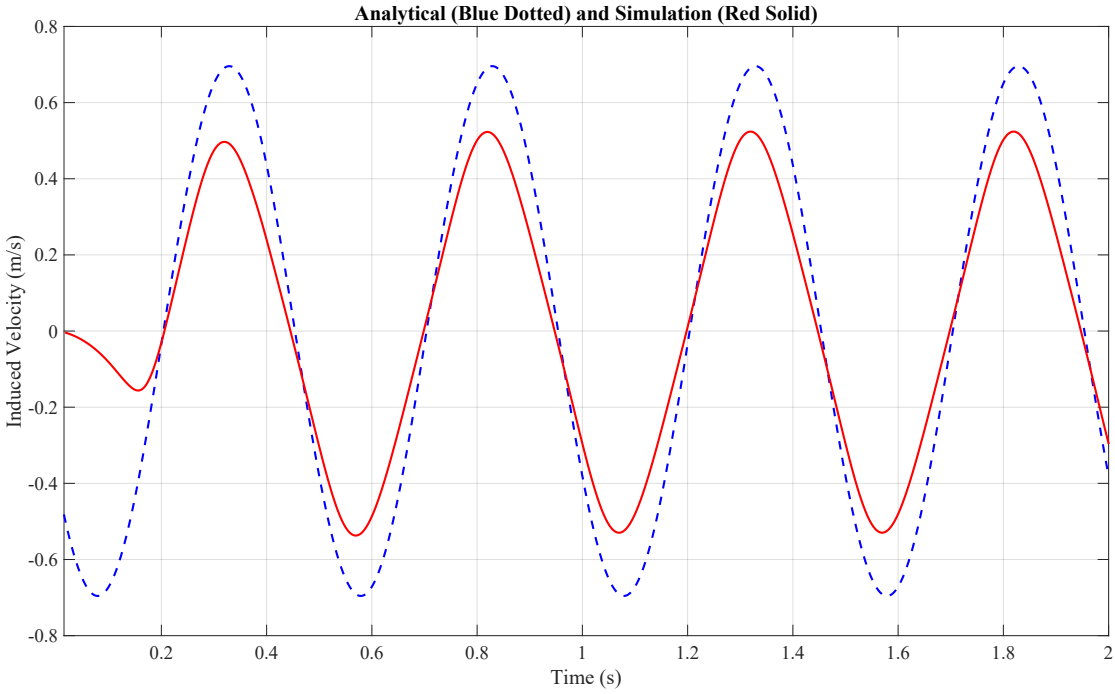

Figure 4.28: Vertical Velocity versus Time for $c = 0.25m$, $f = 2Hz$, $\theta_{max} = 10°$

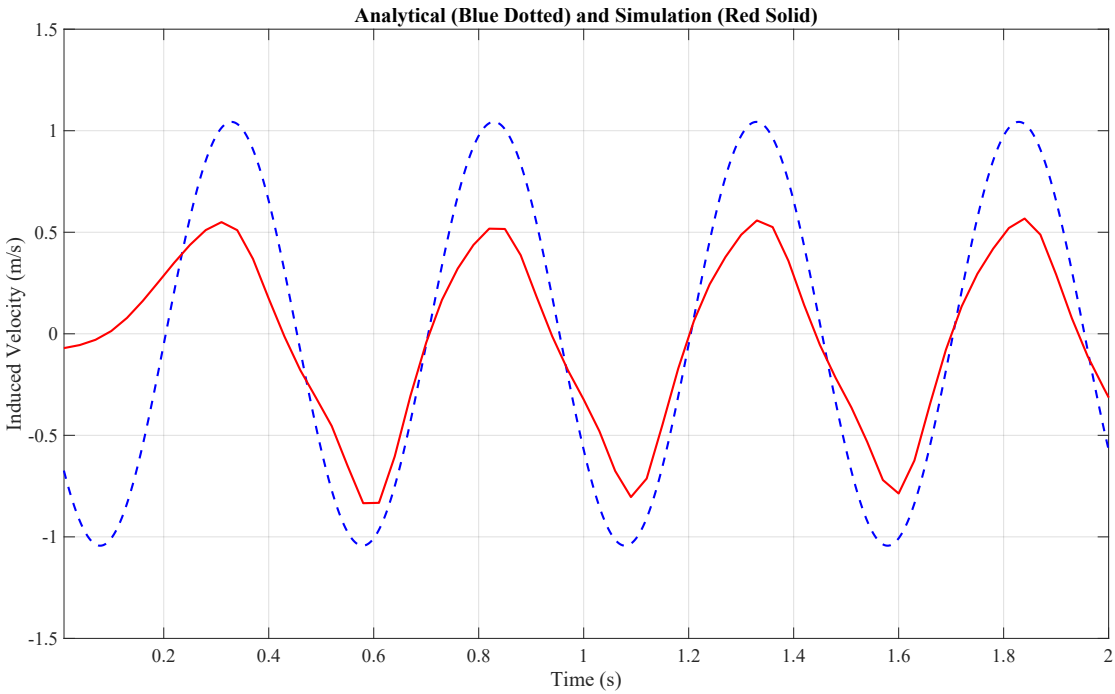

Figure 4.29: Vertical Velocity versus Time for $c = 0.25m$, $f = 2Hz, \theta_{max} = 15°$

4.1.2. Effect of Varying Chord

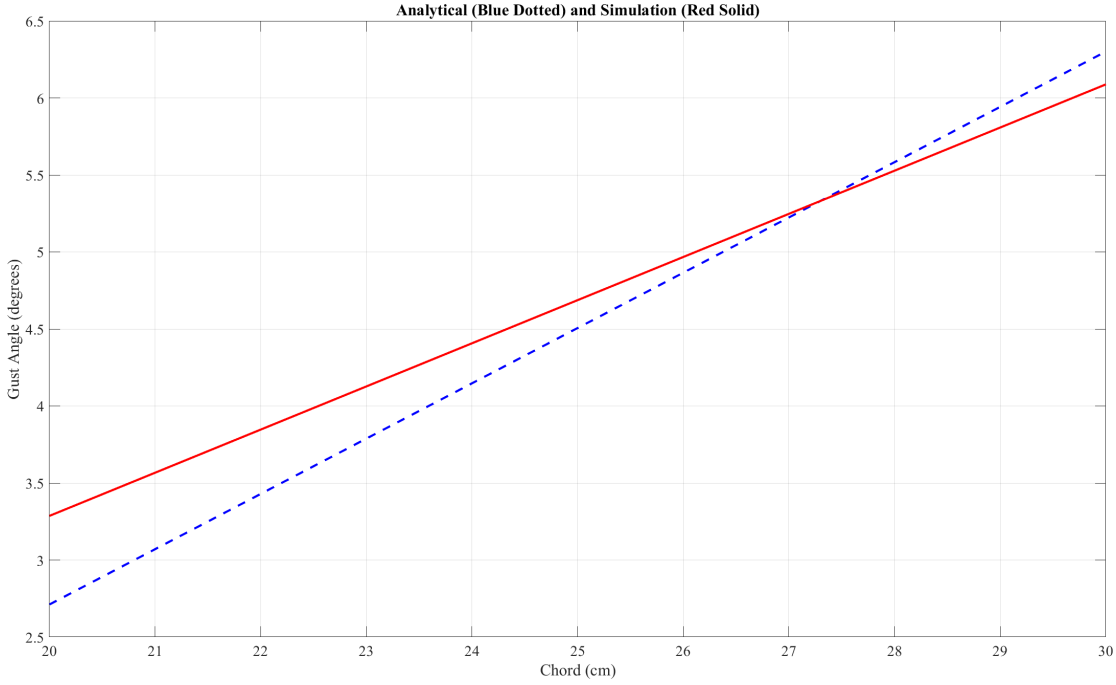

Figure 4.30: Gust Angle versus Chord at $f = 2Hz, \theta_{max} = 10°$

An increase in the gust angle was observed with the increase in the chord length (c). These findings align with the analytical modeling, confirming that if the generated gust

velocity is insufficient, the chord length could be increased. The results also align with the findings of [12], further validating the observed trends.

4.1.3. Effect of Varying Frequency

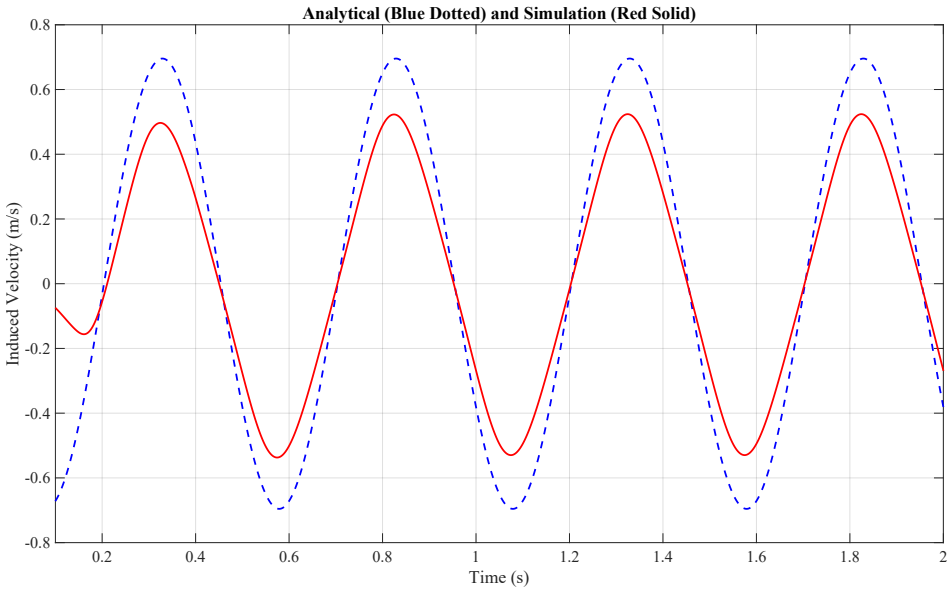

Figure 4.31: Vertical Velocity versus Time at $f = 2Hz, \theta_{max} = 10°$

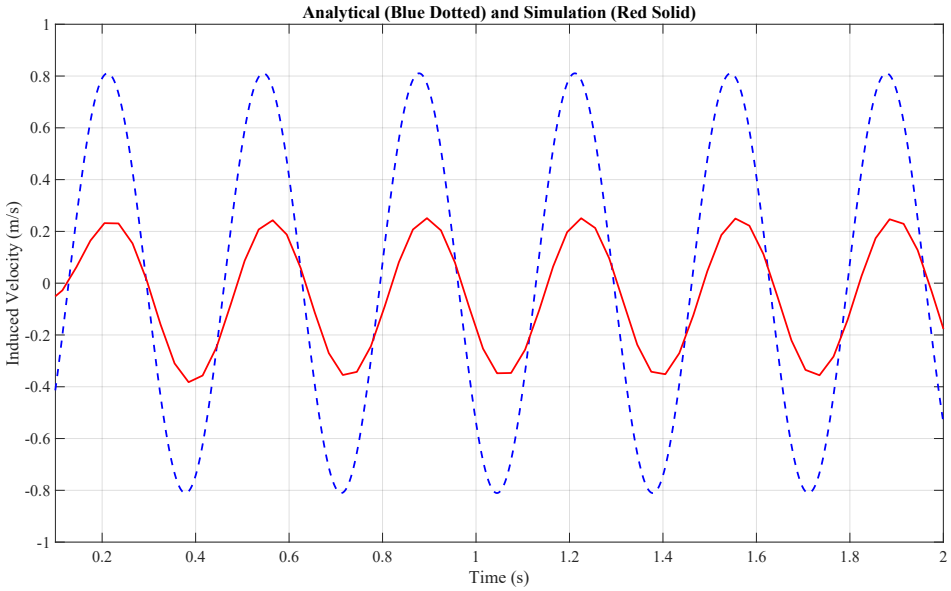

Figure 4.32: Vertical Velocity versus Time at $f = 3Hz, \theta_{max} = 10°$

Increasing the frequency increased the peak magnitude but came with the cost of uniformity. This led to the decrease in the vertical induced velocity due to the introduction of vortices formed. The experiment conducted by Amiralaei et. al. on a pitching NACA 0012 airfoil demonstrated that increasing the amplitude of oscillation leads to stronger

and more extensive vortex generation [32]. When these vortices become more pronounced, gust magnitude increases at the expense of uniformity. This makes gust more variable in magnitude and direction.

The results obtained from simulation and analytical modeling is found to be in accordance with the findings of [32]. Thus, 2 Hz frequency for 25 cm with a deflection angle 10° is seen optimal. Based on the parameters taken, the Strouhal number is calculated as $St = 0.1$.

4.1.4. Experimental Result Before Optimization

The Gust profile obtained is shown in Figure 4.33. The gust profile exhibited sinusoidal nature to a certain degree. However, there was the presence of non-uniformities in the baseline flow at the outlet of the wind tunnel, which was observed as shown in Figure 4.34 without gust generator. This significantly questioned the generated gust profile. As a result, redesigning the wind tunnel to achieve a more reliable gust was deemed necessary.

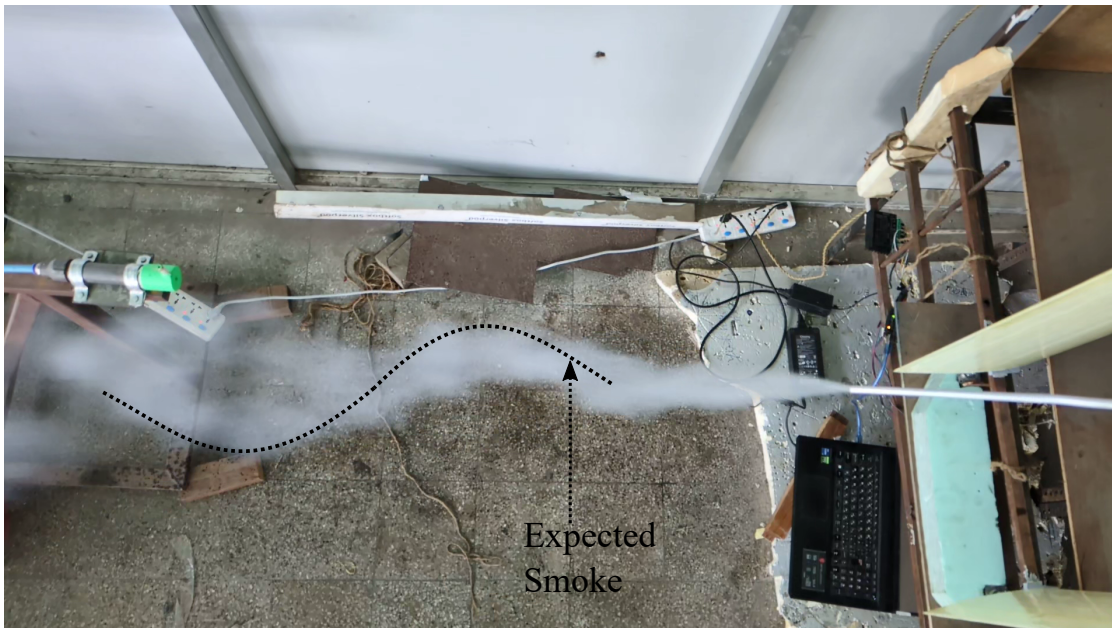

Figure 4.33: Initial Gust Profile (250 cm chord, 2 Hz, 10°, 375 cm spacing)

Figure 4.34: Smoke Visualization for Observing Flow Uniformity at Outlet of the wind tunnel

The smoke produced by the generator was not as dense as desirable for effective gust visualization. The concentration and uniformity of the smoke needed to be increased to improve visualization quality which also necessitated visualization optimization.

The frame and the actuation system presented challenges due to excessive vibration, non-synchronization of the oscillatory motion of the two vanes, and difficulties in setup at the beginning of each experimental observation. Therefore, the frame and the actuation system also needed to be improved to address these issues effectively.

4.2. Outcomes after Optimization

4.2.1. Wind Tunnel Data

The velocity contour for the wind tunnel at the outlet section is obtained as shown in Figure 4.36. Along with this, the velocity contours for the mid-plane of XY and YZ planes as shown in Figure 4.38 and 4.37. The findings suggests that the designed wind tunnel can provide a consistent $10.5\ m/s$ at the outlet region. Figure 4.35 displays the grid convergence for 3D simulation of the tunnel. It shows the test value are not changing much indicating that the solution is nearly grid-independent.

Table 4.11: Grid Independence Study Result

Mesh Type	Mesh Size	Velocity Average	% Reduction
Coarse	853,200	10.17736	-
Medium	2,434,825	10.177608	0.0024
Fine	6,868,800	10.177751	0.0014

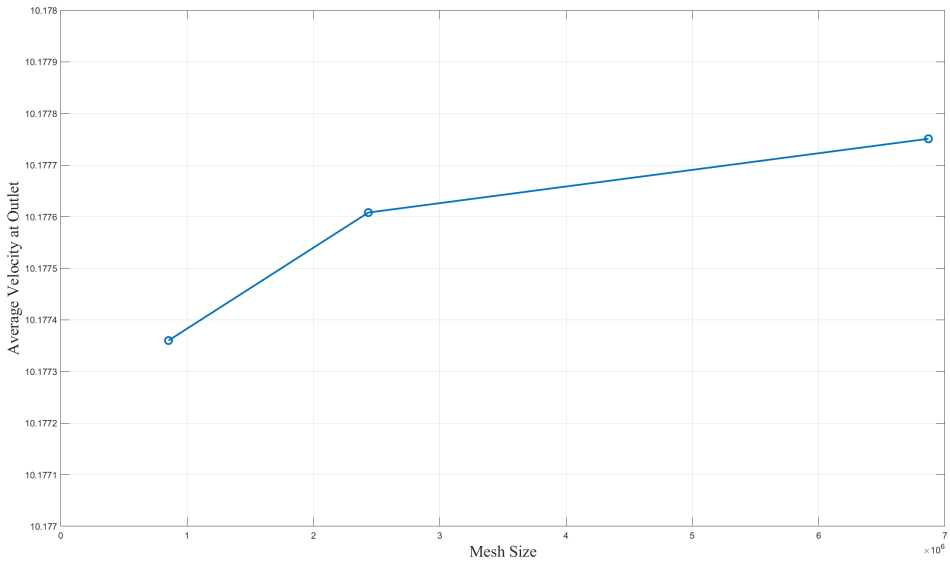

Figure 4.35: Mesh Independence with Richardson Value of Wind Tunnel

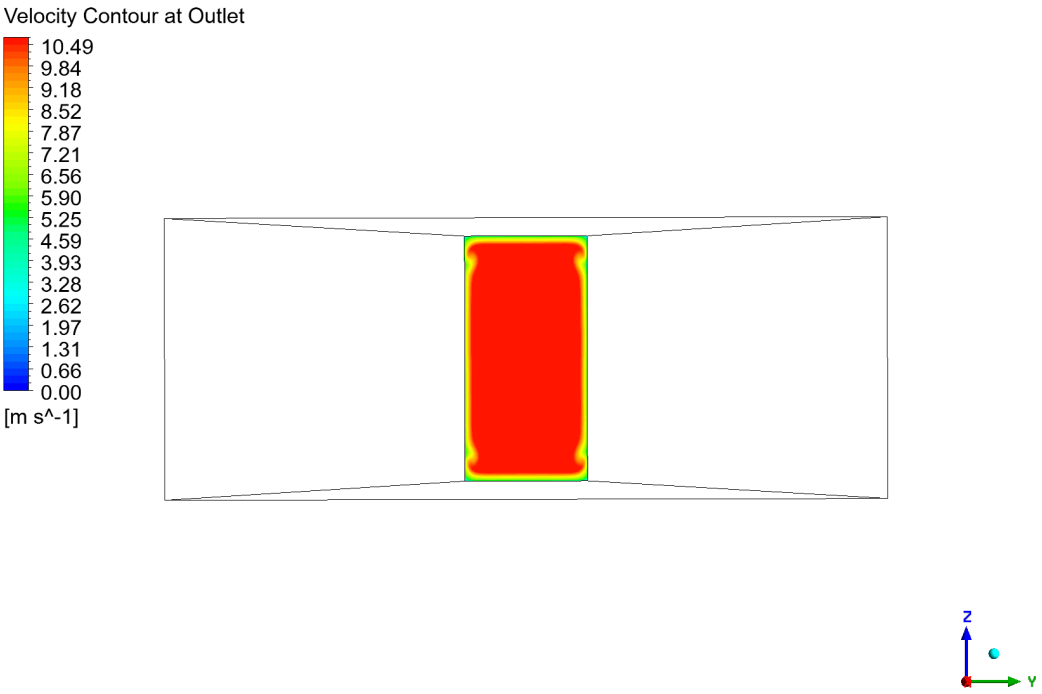

Figure 4.36: Outlet Velocity Contour of the Wind Tunnel

Figure 4.37: XZ Mid Plane Velocity contour

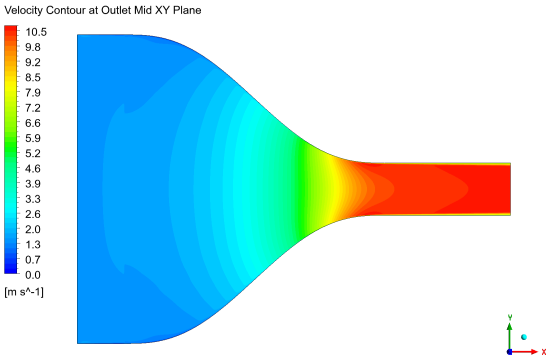

Figure 4.38: XY Mid Plane Velocity contour

At the outlet region, the maximum and minimum velocity contours recorded experimentally are presented in the Figure 4.39 and 4.40. Similarly, the profile was plotted at the test section inside the tunnel as shown in Figure 4.41 and 4.42. The TI was computed for both the outlet & test section using Equation 3.29 and is displayed in Figure 4.43 and 4.44. The averaged values are presented at Appendix B. The value for TI was computed as $2.26\ \%$ at outlet and $0.88\ \%$ at test region. The mean velocities at the outlet and test regions are computed for the purpose of simulation as $8.53\ m/s$ and $8.60\ m/s$.

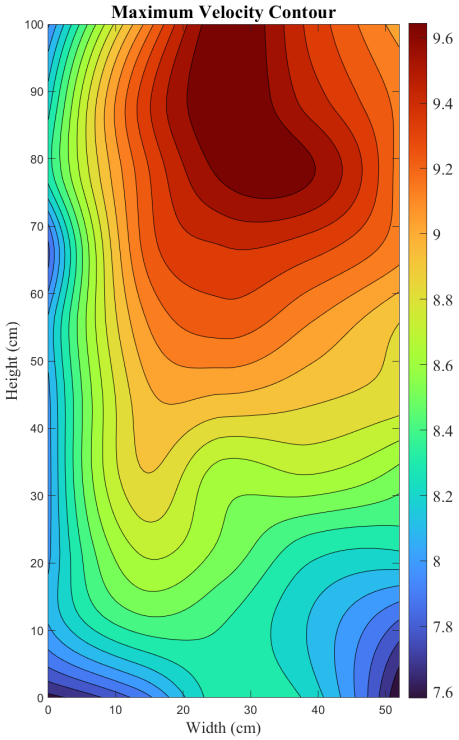

Figure 4.39: Maximum Velocity Contour at Outlet

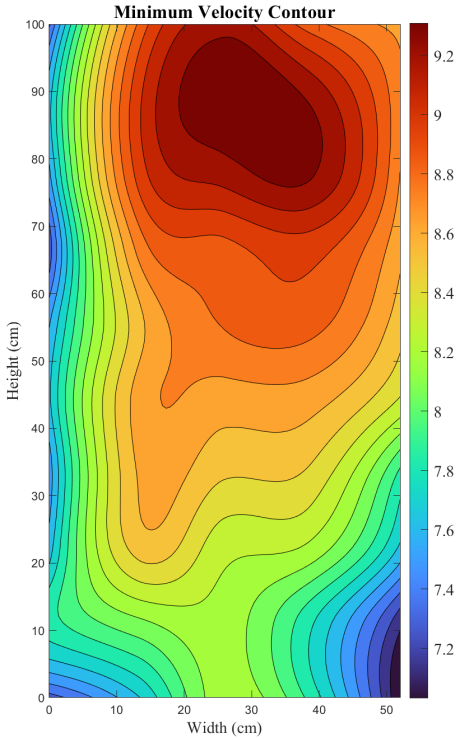

Figure 4.40: Minimum Velocity Contour at Outlet

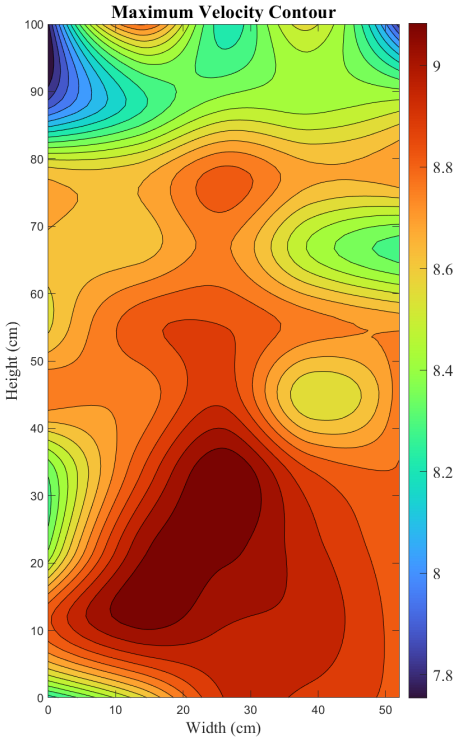

Figure 4.41: Maximum Velocity Contour at Test Section

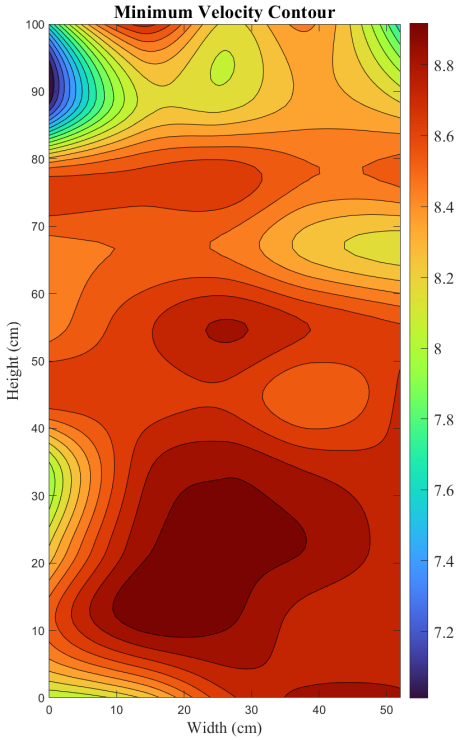

Figure 4.42: Minimum Velocity Contour at Test Section

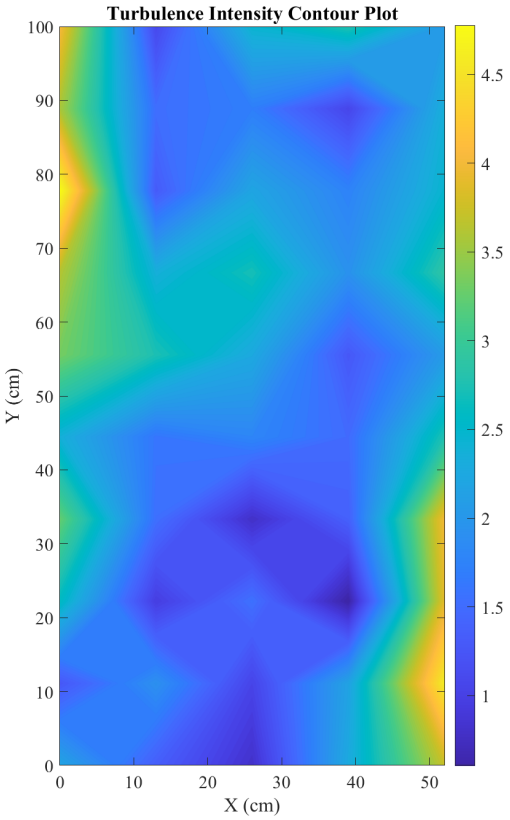

Figure 4.43: TI at Outlet

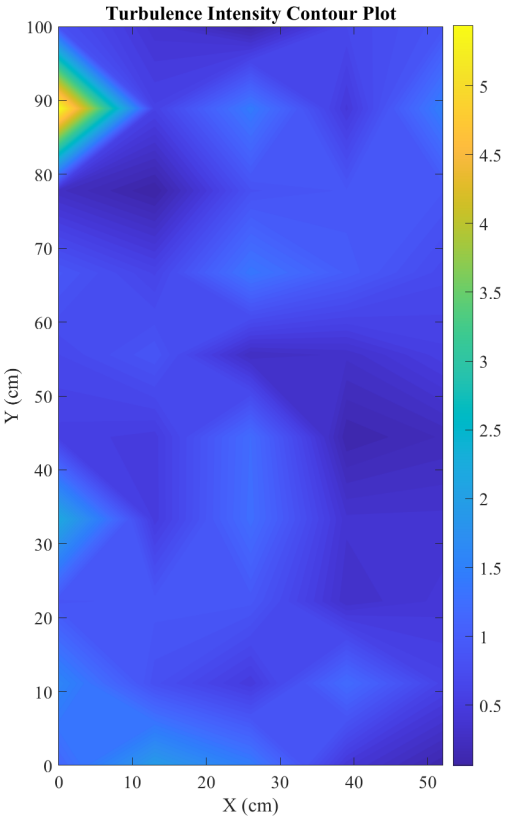

Figure 4.44: TI at Test Section

The error for the velocity obtained at the outlet was determined as follows:

$$\begin{aligned} Error(\%) &= \frac{SimulationVelocity - ExperimentalVelocity}{SimulationVelocity} \times 100 \\ &= \frac{10.17 - 8.54}{10.17} \times 100 \\ &= 16.027\% \end{aligned}$$

Higher turbulence was observed near the walls due to non-smooth contraction curves at the end of the contraction profile. This is due to the approximation fittings of the curve with trapezoidal approximation. To improve the flow uniformity, binding tape was applied to the interior sections of the wind tunnel, while wooden beams were used externally to refine the shape of the contraction profile.

The non uniformity in the velocity both at the outlet and test sections was seen due to the absence of the honeycomb structure at the settling chamber. The newly designed wind tunnel exhibits lower turbulence levels, ensuring a more uniform base flow for efficient gust visualization. Overall, the fabricated wind tunnel (Pulchowk Wind Tunnel (PWT) 2.0) addressed most of the non-uniformity present in Chaudhary's wind tunnel [13].

4.2.2. Gust Experiment

For vanes of $25\ cm$ chord, increasing the frequency of oscillation is seen to improve the profile of sinusoidal gust . At $2\ Hz$, the gust is not very well-defined; $3\ Hz$ shows slight improvement to the profile, $4\ Hz$ produces a good sinusoidal gust, and at $5\ Hz$, further improvement was expected. However, the actuation system was found to limit the smooth oscillation of vanes at this frequency, so it was omitted. Similarly, increasing the deflection angle also improves the gust. At 5°, a weak gust profile is observed; 10° produces better gust profile ; 15° generates a proper sinusoidal gust , and 20° was likely to provide better result. However, 20° again tends to push the actuation system beyond its smooth operating range, so it was omitted. The spacing between vanes also plays a role: $200\ mm$ is seen to produce a weak gust, $300\ mm$ produces better gust profile, but $400\ mm$ was not feasible due to space limitations in the wind tunnel test section, so it could not be tested. Based on these findings, the optimal parameters for the $25\ cm$ chord vanes were determined to be $4\ Hz$, 15° deflection, spaced $300\ mm$ distance apart.

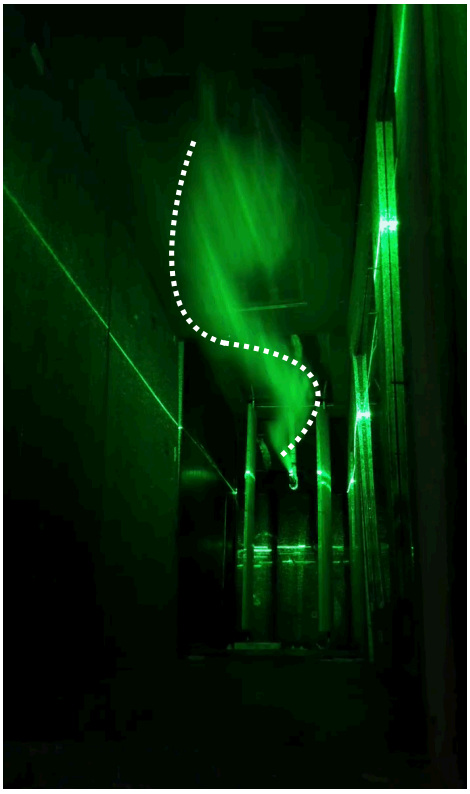

Figure 4.45: Gust Being Developed (4 Hz, 300 mm spacing, 15°, 250 mm chord) at $t = 5.63$ s

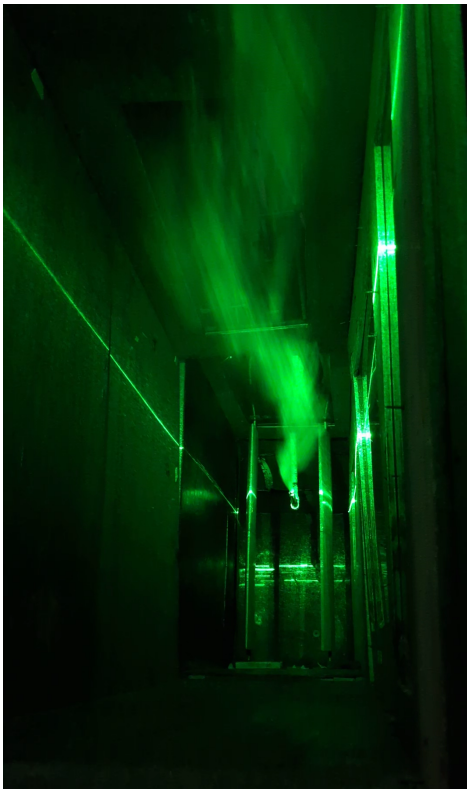

Figure 4.46: Gust Profile(4 Hz, 300 mm spacing, 15°, 250 mm chord) at $t = 11.23$ s

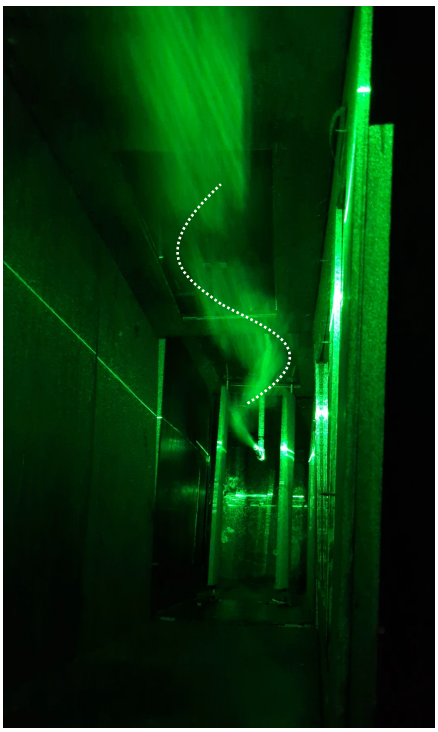

Figure 4.47: Gust Profile (3 Hz, 300 mm spacing, 15°, 250 mm chord) at $t = 20.00$ s

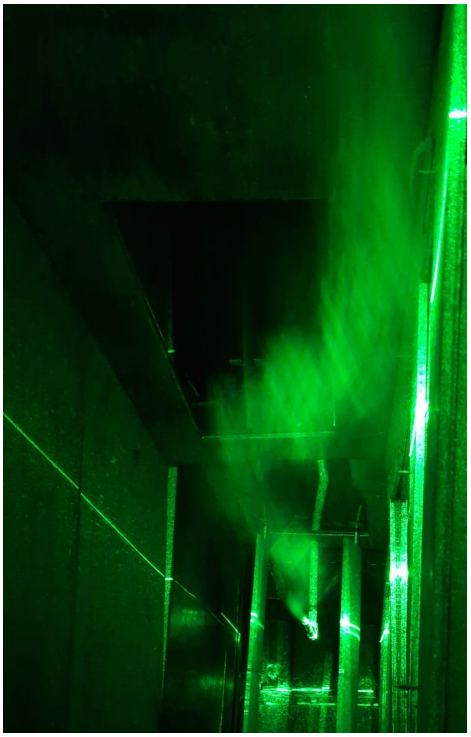

Figure 4.48: Gust Profile (3 Hz, 300 mm spacing, 15°, 250 mm chord) at $t = 22.55$ s

Figure 4.49: Gust Profile ($4Hz$, $200mm$ spacing, $15°$, $250mm$ chord) at $t = 21.62s$

Figure 4.50: Gust Profile ($4Hz$, $200mm$ spacing, $15°$, $250mm$ chord) at $t = 21.65s$

For vanes of $20cm$ chord, smaller spacing of $200mm$ and $300mm$ resulted in highly linear profile of the flow, with no clear sinusoidal behavior. Even increasing the spacing to $400\ mm$ led to only minor improvements. At $4\ Hz$, there was a slight sinusoidal profile. Increasing the deflection even up to $20°$ resulted in the gust remaining mostly linear. Obtaining proper gust profile using $20\ cm$ chord would require higher frequencies, deflections, and spacing, which is not feasible. Hence, $20\ cm$ chord vanes were omitted.

Figure 4.51: Gust Profile ($2\ Hz$, $200\ mm$ spacing, $10°$, $200\ mm$ chord)

Figure 4.52: Gust Profile ($3Hz$, $200mm$ spacing, $10°$, $200mm$ chord)

Figure 4.53: Gust Profile ($4\ Hz$, $200\ mm$ spacing, $15°$, $200\ mm$ chord)

Figure 4.54: Gust Profile ($4Hz$, $300mm$ spacing, $15°$, $200mm$ chord)

While the $30cm$ chord configuration was expected to yield better results, it was omitted as the actuation system could not provide sufficient power for its operation. This project successfully observed the $1 - cosine$ gust profile experimentally. Gust visualization was conducted qualitatively using smoke and laser-based techniques.

4.2.3. Gust Simulation & Analytical Result

The grid independence study for the gust simulation is shown in Table 4.12. The maximum vertical induced velocity from the fine mesh is computed as $1.29m/s$. Also, the analytical model for this grid was done as shown in Figure 4.55. The error obtained from the simulation and analytical is computed as 10.63% at ($t = 0.41s$). The induced vertical velocity shows a strong correlation between the simulation and analytical results at the selected optimal parameters.

Table 4.12: Grid Independence Study Result for Gust Simulation

Label	**Number of Elements**	**Maximum Vertical Induced Velocity**	**Percentage Reduction (%)**
Coarse	51,475	1.824	-
Medium	130,105	1.621	11.04
Fine	216,859	1.641	1.218

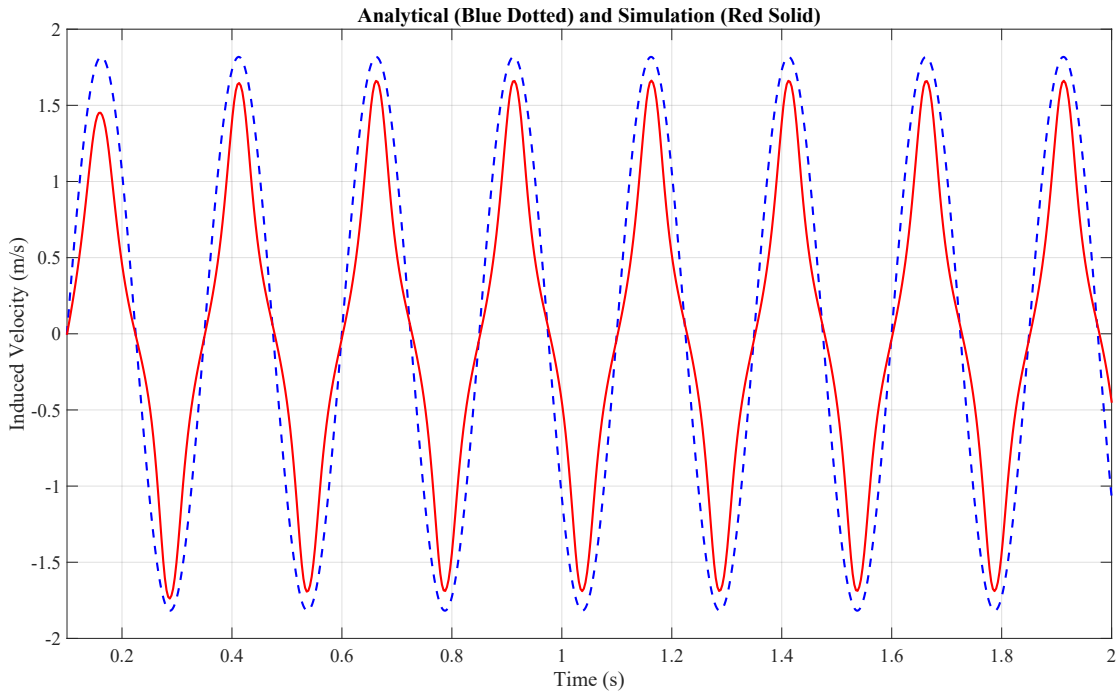

Figure 4.55: Comparison of Analytical and Simulation Result

For vanes configuration of chord $20cm$ oscillating with a frequency of $2Hz$ oscillation frequency at a $10°$ deflection angle, the results show that at $100cm$ spacing, the gust velocity is the highest. However, due to the limited spacing, there was significant wake interactions between the vanes, which causes non-uniformity in the generated gust. Increasing the spacing to $200cm$ results in lower gust velocity but improved gust uniformity. At a spacing of $300\ mm$, the flow remained more stable with minimal wake interactions, ensuring a smoother gust profile. This highlights the trade-off between gust magnitude and uniformity at various spacing. The results are in agreement with those concluded by [12].

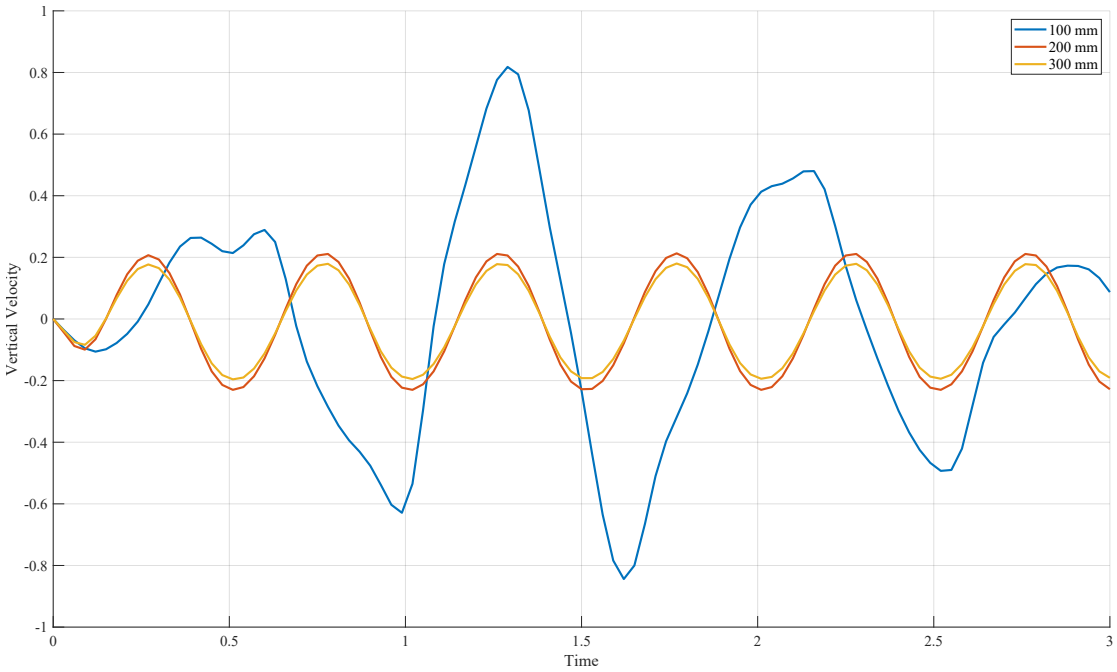

Figure 4.56: Effect of Spacing on Vertical Velocity for $20cm$ chord $(2Hz, 10°)$

4.2.4. Gust Characterization

The gust generated was qualitatively characterized. The captured gust video was post-processed and converted into individual frames. A specific frame corresponding to a time of 3.26 seconds after gust initiation was selected for analysis. The wavelength of one complete gust cycle was measured using the background of extended test section mirror as a reference, whose physical length is known to be 96 cm. By comparing the number of pixels corresponding to the known mirror length as shown in Figure 4.57, the pixel length of the gust wavelength was measured and then scaled to obtain its actual physical magnitude.

The experimentally measured wavelength was found to be 208.437 cm. To validate this result, the theoretical wavelength was calculated using the relation:

$$\lambda = \frac{U}{f}$$

where λ is the wavelength, U is the free-stream velocity (8.6 m/s), and f is the gust frequency (4 Hz). The resulting theoretical wavelength is 215 cm. The percentage error was calculated to be 3.05%, validating the accuracy of the observed gust profile. Figure 4.59 represents the sinusoidal nature of the generated gust.

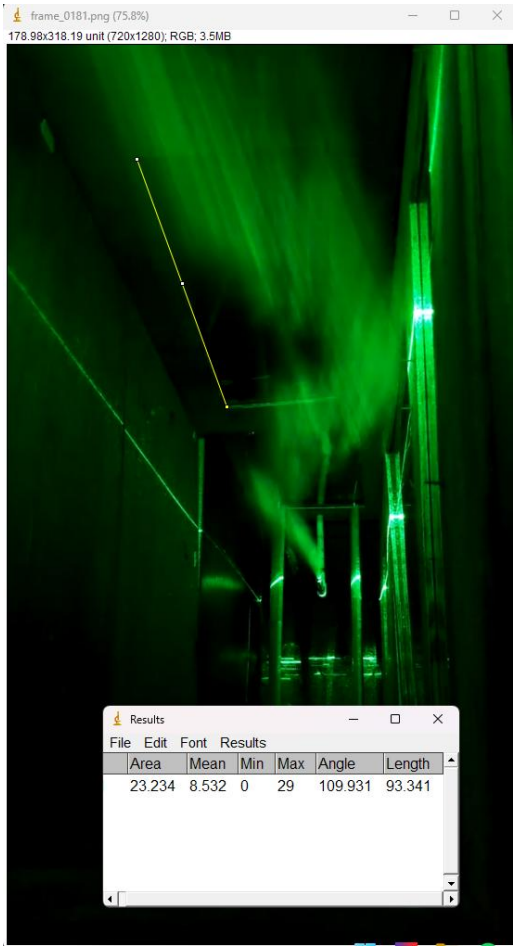

Figure 4.57: Setting the scale

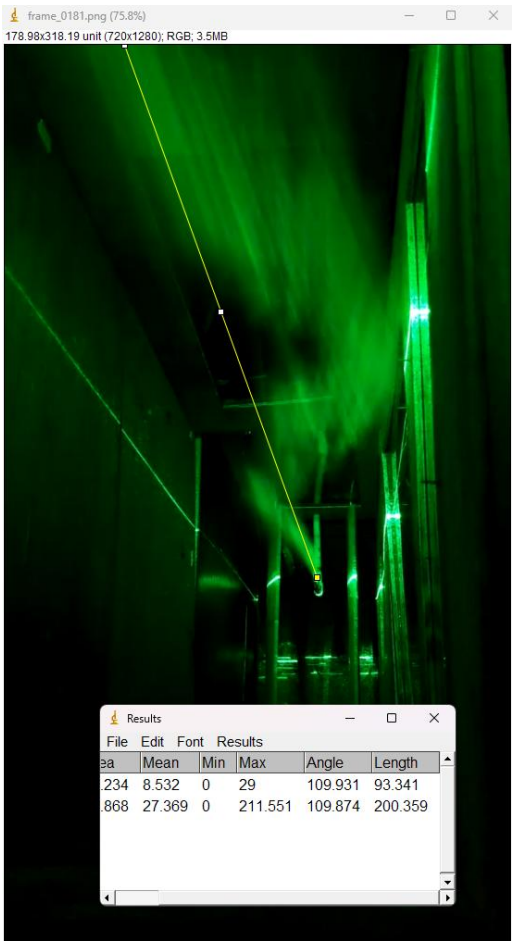

Figure 4.58: Measuring wavelength

Figure 4.59: Sinusoidal Profile

4.3. Utilization of Wind Tunnel and Gust Generator

The developed wind tunnel and gust generator has been utilized by various other project teams, which shows further applications and widens the scope of our project.

1. Project group performing " Experimental Study of Leading Edge Sinusoidal Tubercles on NACA 63215 Wing at Low Reynolds Number" utilized the wind tunnel to calibrate load cell to validate the increase in stall angle by introducing Tubercles in contrast to traditional wing as shown in Figure C.15.

2. Project group performing "Fabrication, Structural Integrity and Dynamic Response of a Carbon Fiber Wing With Study on Material Properties and Vibration Characterization" utilized the wind tunnel to perform vibration analysis on a composite wing as shown in Figure C.18.

3. Project group performing implementation of Digital Twin Technology for Aircraft Wing's Real-Time Structural Health Monitoring" utilized the wind tunnel to calculate structural deformation on the wing obtained by the tunnel airflow as shown in Figure C.17.

4. Project group performing "Integrated Control System for Active Fin Controlled stabilization and Guidance of a Rocket" utilized the wind tunnel to study pitch optimization through automatic fin actuation of rocket as shown in Figure C.16. The effect of gust on the fin deflection was also observed. The introduction of gust led to higher deflection of the rocket fin to obtain desired pitch of 15°.

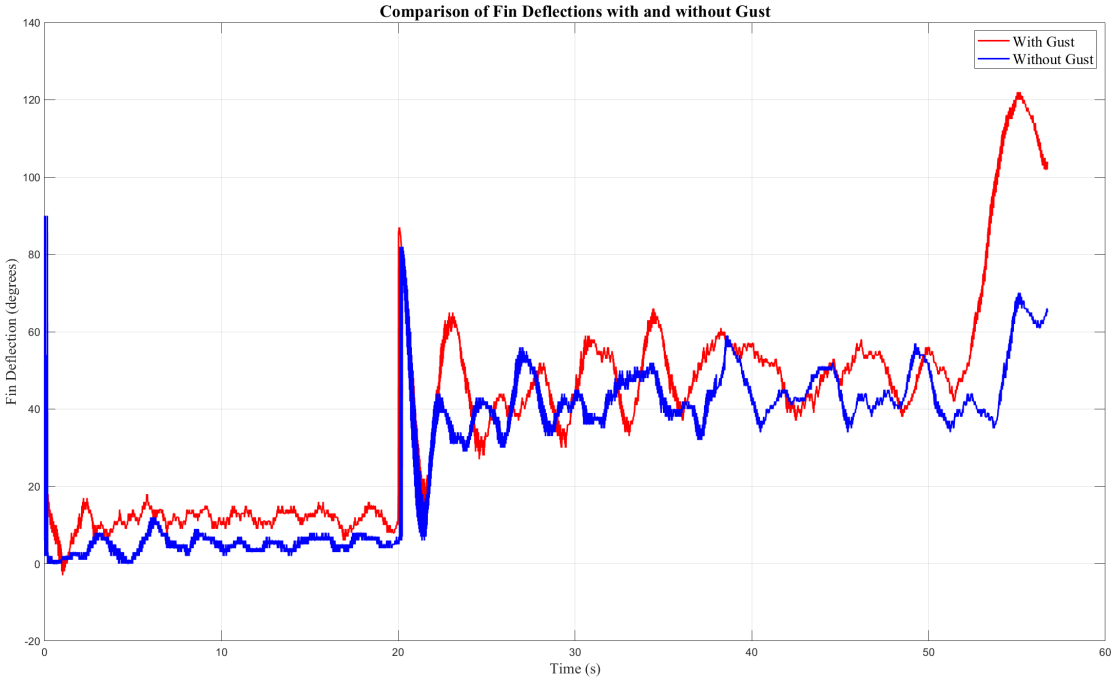

Figure 4.60: Fin Deflection Angle for Rocket with and without gust

4.4. Limitations

The main limitations of the project are listed below:

1. **Hot wire Anemometer:**

   The lack of a hot-wire anemometer made it difficult to validate the induced gust velocity against the simulation and analytical models, which in turn made it harder to accurately characterize the gust profile quantitatively.

2. **Actuation:**

   The limitations of the stepper motor caused jerking motion during vane oscillation, which impacted the smoothness and accuracy of the gust generation. Using a more powerful stepper motor along with better driver like DM556T could help achieve smoother and more consistent actuation.

4.5. Problems Encountered

The various problems encountered in the duration of the project are listed below.

1. **Actuation Issues:**

The selected NEMA 23 stepper motor was unable to provide the necessary torque for oscillation of vanes at higher frequency and degree of oscillation. This led to inconsistent vane motion, affecting the accuracy of gust generation. The stepper motor driver introduced excessive vibrations which also caused mechanical instability. This affected the sinusoidal nature of the gust profile achievable.

2. **Frame Stability:**

   The initial frame design did not provide sufficient rigidity, causing excessive vibration of the vanes during oscillation. This affected the accuracy of vane oscillations and overall experimental reliability while causing delay in the smooth progress of the project, as much of the time was taken up integrating the frame into the wind tunnel to limit vibration.

3. **Wind Tunnel Non-uniformities:**

   Flow non-uniformities which were observed at the previous wind tunnel outlet affected the proper formation of initial gust profiles visualized. This required modifications to the tunnel design. This delayed progress in gust visualization.

4. **Smoke Intensity:**

   The smoke generator produced smoke intensity was inconsistent and insufficient , making it difficult to effectively visualize the flow characteristics. Improvements in the smoke injection method was needed to improve visualization.

4.6. Budget Analysis

The total budget used for this project is around **NPR. 34,000** and is shown in Table 4.13. It has been described in detail in Table B.1.

Table 4.13: Financial Distribution Across Categories

Category	**Amount Nrs.**
Chemical	5,408
Electronics	2,500
Hardware	23,974
Miscellaneous	1,690
Grand Total	**33571.85**

4.7. Work Schedule

The work conducted for this project throughout the year is presented in Figure 4.61 as described by Table B.10. They have been categorized into subtasks. Each of them have been given respective duration for their completion.

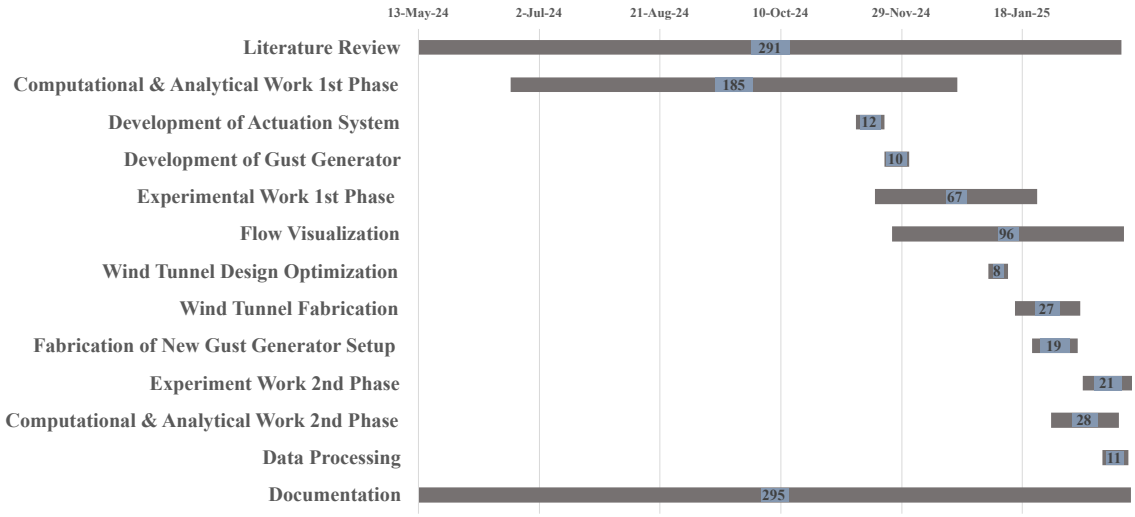

Figure 4.61: Project Timeline Chart

CHAPTER FIVE: CONCLUSION AND FUTURE ENHANCEMENT

5.1. Conclusion

The project of developing a wind tunnel with integrated oscillating vanes to generate a sinusoidal gust profile and perform smoke visualization for qualitative analysis was successfully completed. The parameters for vane oscillation were systematically varied. The vertical induced velocity at ($x = 1\ m$, $y = 0\ m$) from the LE obtained from simulation and analytical methods showed good agreement, which was used to select an optimal set of parameters. Experimental tests were conducted with smoke visualization. However, the sinusoidal profile was not highly pronounced.

To address flow non-uniformity, the wind tunnel design was optimized, achieving a TI of 0.88% at the test section and 2.26% at the outlet, with a calculated outlet error of 16.027% using simulation with a mean velocity of $8.6\ m/s$. Experimental tests were repeated with varying parameters to obtain refined set of optimal parameters ($25\ cm$ chord, $4\ Hz$ frequency, $15°$ deflection, and $300\ mm$ spacing). The Re is calculated to be 147186.21, St as 0.116, and k as 0.365. Simulations and analytical modeling were performed with the optimal parameters. The results for the induced vertical velocity at ($x = 1\ m$, $y = 0\ m$) from the LE showed an error of 10.63%. The wavelength of the generated gust of $4Hz$ has been calculated to be $208.437\ cm$ with an error of $3.05\ \%$.

Gust visualization using smoke and a plane laser confirmed a sinusoidal gust profile qualitatively. However, proper quantitative characterization could not be done due to the unavailability of a hot-wire anemometer, which would have allowed direct experimental validation. Future work can include quantitative gust characterization and Particle Tracking Velocimetry (PTV) for better gust analysis. The developed wind tunnel and gust generator offer significant potential for aerodynamic studies and testing.

5.2. Scope for Future Enhancement

Our project provides a functional gust generator integrated into a low-subsonic wind tunnel, with numerous potential for further refinement and optimization. Several methods exist for improving both the efficiency and the precision of the system, which could enhance its overall performance.

i. **Horizontal Vanes:** To increase the gust amplitude, it was necessary to increase the number of vanes. However, due to space limitations in the outlet section of the wind tunnel, only four vanes could be used. Also, increasing spacing was not feasible. This could be achieved using horizontal vanes for the designed wind tunnel, which can be actuated using a crank-rocker linkage mechanism.

ii. **Flow Visualization Techniques:** The incorporation of advanced flow visualization techniques, such as Particle Tracking Velocimetry (PTV), to obtain more detailed velocity field measurements and obtain more reliable quantitative gust characterization can be done.

iii. **Smoke Streamline Visualization:** Improving smoke injection techniques to generate proper and smooth streamlines for better flow visualization and analysis of gust effects can be done. Air Compressor can be used to pass the smoke for increasing the intensity rather than a duct fan.

iv. **Wind tunnel Inlet:** The flow at the outlet, although better than the previous wind tunnel, is still non-uniform. This could be made more uniform by adding a diffuser section after the inlet. However, this would have required modifying the inlet section itself by giving it a octagonal shape. This could be taken up as a part of future project to optimize the wind tunnel flow uniformity at the outlet.

v. **Honeycombs and Screens:** Adding honeycomb structures and screens at the wind tunnel settling chamber to further reduce turbulence intensity and improve flow uniformity for better experimental observations can be done.

REFERENCES

[1] A. R. Jones, O. Cetiner, and M. J. Smith, "Physics and modeling of large flow disturbances: discrete gust encounters for modern air vehicles," *Annual Review of Fluid Mechanics*, vol. 54, pp. 469–493, 2022, doi: 10.1146/annurev-fluid-031621-085520.

[2] M. Vlajinac, "Design, construction and evaluation of a subsonic wind tunnel." Ph.D. dissertation, Massachusetts Institute of Technology, 1970.

[3] T. Z. Zhenlong Wu, Y. Gao, and H. Tan, "Development of a novel small-scale gust generator research facility," *Aerospace*, vol. 11, no. 1, p. 95, 2024, doi: 10.3390/aerospace11010095.

[4] Z. Wu, Y. Cao, and M. Ismail, "Gust loads on aircraft," *The Aeronautical Journal*, vol. 123, no. 1266, pp. 1216–1274, 2019, doi: 10.1017/aer.2019.48.

[5] J. K. ZBROZEK, "Atmospheric turbulence and its relation to aircraft," *Nature Publishing Group UK London*, vol. 193, no. 4819, p. 933–934, 1962, doi: 10.1038/193933a0.

[6] "14 cfr 25.341," eCFR, 2024, (Accessed May 30, 2024). [Online]. Available: https://www.ecfr.gov/current/title-14/part-25/section-25.341

[7] R. L. Bisplinghoff and H. Ashley, *Principles of aeroelasticity*. Courier Corporation, 2013.

[8] T. Theodorsen, "General theory of aerodynamic instability and the mechanism of flutter," Tech. Rep., 1979.

[9] M. Lab, "Bessel functions of the first and second kind," https://www.mhtlab.uwaterloo.ca/courses/me755/web_chap4.pdf, n.d., accessed: 2024-12-17.

[10] J. Anderson, *Fundamentals of Aerodynamics*, ser. McGraw-Hill Aeronautical and aerospace engineering series. McGraw-Hill, 1991. [Online]. Available: https://books.google.com.np/books?id=LJ-hAAAACAAJ

[11] M. S. U. Khalid, I. Akhtar, and N. I. Durrani, "Analysis of strouhal number based equivalence of pitching and plunging airfoils and wake deflection," *Proceedings of the Institution of Mechanical Engineers, Part G: Journal of Aerospace Engineering*, vol. 229, no. 8, pp. 1423–1434, 2015.

[12] P. M. Lancelot, J. Sodja, N. P. Werter, and R. De Breuker, "Design and testing of a low subsonic wind tunnel gust generator," *Advances in aircraft and spacecraft science*, vol. 4, no. 2, p. 125, 2017, doi: 10.12989/aas.2017.4.2.125.

[13] R. Chaudhary, "Design, fabrication and performance evaluation of low speed open jet wind tunnel for free flight test of a glider," 2023.

[14] M. S. Genç, İ. Karasu, and H. H. Açıkel, "An experimental study on aerodynamics of naca2415 aerofoil at low re numbers," *Experimental Thermal and Fluid Science*, vol. 39, pp. 252–264, 2012.

[15] J. B. Barlow, W. H. Rae, and A. Pope, *Low-speed wind tunnel testing*. John wiley & sons, 1999.

[16] S. Mauro, S. Brusca, R. Lanzafame, F. Famoso, A. Galvagno, M. Messina *et al.*, "Small-scale open-circuit wind tunnel: Design criteria, construction and calibration," *International Journal of Applied Engineering Research*, vol. 12, no. 23, pp. 13 649–13 662, 2017.

[17] R. D. Mehta and P. Bradshaw, "Design rules for small low speed wind tunnels," *The Aeronautical Journal*, vol. 83, no. 827, pp. 443–453, 1979.

[18] O. d. Almeida, F. C. d. Miranda, O. Ferreira Neto, and F. G. Saad, "Low subsonic wind tunnel-design and construction," *Journal of Aerospace Technology and Management*, vol. 10, p. e1018, 2018.

[19] J. H. Bell and R. D. Mehta, "Contraction design for small low-speed wind tunnels," Tech. Rep., 1988.

[20] M. Arifuzzaman and M. Mashud, "Design construction and performance test of a low cost subsonic wind tunnel," *IOSR Journal of Engineering*, vol. 2, no. 10, pp. 83–92, 2012.

[21] R. Loehrke and H. M. Nagib, "Experiments on management of free-stream turbulence." AGARD, 1972.

[22] C. Farell and S. Youssef, "Experiments on turbulence management using screens and honeycombs," 1996.

[23] A. French, W. Friess, A. Goupee, and K. Berube, "Design, construction and evaluation of an oscillating vane gust generator for atmospheric flow simulation," *Wind*, vol. 1, no. 1, pp. 63–76, 2021, doi: 10.3390/wind1010004.

[24] K. T. Wood, R. C. Cheung, T. S. Richardson, J. E. Cooper, O. Darbyshire, and C. Warsop, "A new gust generator for a low speed wind tunnel: Design and commissioning." American Institute of Aeronautics and Astronautics, 2017, doi: 10.2514/6.2017-0502.

[25] Z. Wu, T. Zhang, Y. Gao, and H. Tan, "Development of a novel small-scale gust generator research facility," *Aerospace*, vol. 11, no. 1, p. 95, 2024, doi: 10.3390/aerospace11010095.

[26] A. French, *Investigation of Infiltration Measurements Using Wind Induced Pressure Response on an Enclosure*. The University of Maine, 2020. [Online]. Available: https://digitalcommons.library.umaine.edu/etd/3162

[27] D. Tang and E. H. Dowell, "Experimental and theoretical study of gust response for high-aspect-ratio wing," *AIAA journal*, vol. 40, no. 3, pp. 419–429, 2002, doi: 10.2514/2.1691.

[28] J. Neumann and H. Mai, "Gust response: Simulation of an aeroelastic experiment by a fluid–structure interaction method," *Journal of Fluids and Structures*, vol. 38, pp. 290–302, 2013, doi: 10.1016/j.jfluidstructs.2012.12.007.

[29] D. Tang, P. G. Cizmas, and E. Dowell, "Experiments and analysis for a gust generator in a wind tunnel," *Journal of Aircraft*, vol. 33, no. 1, pp. 139–148, 1996, doi: 10.2514/3.46914.

[30] N. T. Nguyen, J. Xiong, and N. B. Cramer, "Simulation and modeling of flow generated by gust generator in a wind tunnel," in *AIAA SciTech 2020 Forum*, 2020, p. 0212.

[31] İ. YIĞILI, M. ANDIRIN, E. Kurban, Ö. BAŞKAN PERÇİN, and M. PERÇİN, "Design and experimental investigation of a wind tunnel gust generator," 2021.

[32] M. Amiralaei, H. Alighanbari, and S. Hashemi, "An investigation into the effects of unsteady parameters on the aerodynamics of a low reynolds number pitching airfoil," *Journal of Fluids and Structures*, vol. 26, no. 6, pp. 979–993, 2010.

APPENDIX A: COMPUTATIONAL CODES

User-Defined Function for SHM Motion for Airfoil

Listing 1: UDF Code for SHM Motion of Airfoil

```
#include "udf.h"
#define Freq 2.0
#define angular_freq 2.0*M_PI*Freq
#define tetmax 10.0*M_PI/180

DEFINE_CG_MOTION(shm, dt, cg_vel, cg_omega, time, dtime)
{
  real omega;
  omega = tetmax * angular_freq * cos(angular_freq * time);

  cg_vel[0] = 0.0;
  cg_vel[1] = 0.0;
  cg_vel[2] = 0.0;

  cg_omega[0] = 0.0;
  cg_omega[1] = 0.0;
  cg_omega[2] = omega;
}

}
```

Stepper Motor Arduino Code

Listing 2: Arduino Code for Stepper Motor

```
const int stepPin = 5;
const int dirPin =2;
const int enPin = 8;

void setup(){
  pinMode(stepPin, OUTPUT);
  pinMode(dirPin, OUTPUT);

  pinMode(enPin, OUTPUT);
  digitalWrite(enPin, LOW);

}
```

```
void loop()
{
  digitalWrite(dirPin, HIGH);

  for(int x=0;x<267;x++){
    digitalWrite(stepPin,HIGH);
    delayMicroseconds(234);
    digitalWrite(stepPin, LOW);
    delayMicroseconds(234);
  }
  delay(0);
  digitalWrite(dirPin, LOW);

  for(int x=0;x<267;x++){
    digitalWrite(stepPin,HIGH);
    delayMicroseconds(234);
    digitalWrite(stepPin, LOW);
    delayMicroseconds(234);
  }
  delay(0);
}
```

Comparison of Analytical & Simulation Code for Deflection Angle and Frequency

Listing 3: Analytical Code to Compare with Simulation

```
clc;
clear all;
close all;

filename = 'fine.csv';
data = readmatrix(filename);
x_csv = data(:, 1);
y_csv = data(:, 2);

[~, idx_1sec_csv] = min(abs(x_csv - 1));
x_1sec_csv = x_csv(idx_1sec_csv);
y_1sec_csv = y_csv(idx_1sec_csv);

U_inf = 8.6;
c = 0.25;
alpha_0 = deg2rad(15);
```

```
f = 4;
omega = 2 * pi * f;
k = (omega * c) / (2 * U_inf);

separation = 0.3;
num_airfoils = 2;

dt = 0.002;
t = 0:dt:2;

x_point = 1;
y_point = 0;

H0 = besselh(0, 2, k);
H1 = besselh(1, 2, k);
C_k = H1 / (H0 + 1i * H1);

phase_correction = pi / 2;

v_total = zeros(size(t));

for i = 1:num_airfoils
x_airfoil = (i - 1.5) * separation;
z = (x_point - x_airfoil) + 1i * y_point;
Gamma = 2 * pi * alpha_0 * U_inf * c * C_k .* exp(1i * ...
(omega * t + phase_correction));
v_induced = imag(-Gamma ./ (2 * pi * z.^2));
v_total = v_total + v_induced;
end

[~, idx_1sec_analytical] = min(abs(t - 1));
t_1sec_analytical = t(idx_1sec_analytical);
v_1sec_analytical = v_total(idx_1sec_analytical);

figure;

plot(t, v_total, 'b--', 'LineWidth', 2, 'DisplayName',
   'Analytical');
hold on;
plot(x_csv, y_csv, 'r-', 'LineWidth', 2, 'DisplayName',
   'Simulation');
```

```
xlim([0 2]);

xlabel('Time (s)', 'FontSize', 20, 'FontName', 'Times New
    Roman');
ylabel('Induced Velocity (m/s)', 'FontSize', 20, 'FontName',
    ...
'Times New Roman');
title('Analytical (Blue Dotted) and Simulation (Red Solid)',
    'FontSize', ...
18, 'FontName', 'Times New Roman');
set(gca, 'FontSize', 18, 'FontName', 'Times New Roman');
grid on;
hold off;
```

Average Velocity Code for the Wind Tunnel

Listing 4: Average Velocity

```
data1 = load('data1.mat');
data2 = load('data2.mat');
data3 = load('data3.mat');

data1 = data1.data;
data2 = data2.data;
data3 = data3.data;

averageData = (data1 + data2 + data3) / 3;

disp('The average data is:');
disp(averageData);
```

Contour Plot Code for the Wind Tunnel

Listing 5: Contour Plot

```
close all;
clear;

dataStruct = load('data.mat');
velocity = dataStruct.data;

ny = size(velocity, 1);
nx = size(velocity, 2);
```

```
Lx = 52;
Ly = 100;

x = linspace(0, Lx, nx);
y = linspace(0, Ly, ny);

%smoothness
nx_fine = 100;
ny_fine = 100;

x_fine = linspace(0, Lx, nx_fine);
y_fine = linspace(0, Ly, ny_fine);
[X_fine, Y_fine] = meshgrid(x_fine, y_fine);

velocity_fine = interp2(x, y, velocity, X_fine, Y_fine,
    'cubic');

figure;
contourf(X_fine, Y_fine, velocity_fine, 20);
colormap(turbo);
colorbar;
cb = colorbar;
cb.FontSize = 14;
cb.FontName = 'Times New Roman';
xlabel('Width (cm)', 'FontSize', 14, 'FontName', 'Times New
    Roman');
ylabel('Height (cm)', 'FontSize', 14, 'FontName', 'Times New
    Roman');
title('Minimum Velocity Contour', 'FontSize', 16, 'FontName',
    'Times New Roman');
pbaspect([52/100, 1, 1]);

set(gca, 'YDir', 'normal');
```

TI Calculation and Contour Code for th Wind Tunnel

Listing 6: TI calculation

```
clear;
close all;
load('maximum.mat');
load('minimum.mat');
```

```
5
6  U_mean = (maximum + minimum) / 2;
7  very_mean = mean(U_mean(:));
8
9  u_prime = maximum - U_mean;
10
11 turbulent_intensity_grid = (u_prime ./ U_mean) * 100;
12
13 average_turbulent_intensity =
       mean(turbulent_intensity_grid(:));
14 disp(['Mean Velocity: ',num2str(very_mean)]);
15
16 disp(['Average Turbulent Intensity: ',
       num2str(average_turbulent_intensity) , '%']);
17
18 x_actual = linspace(0, 52, size(turbulent_intensity_grid, 2));
19 y_actual = linspace(0, 100, size(turbulent_intensity_grid, 1));
20
21 figure;
22 contourf(x_actual, y_actual, turbulent_intensity_grid, 100,
       'LineColor', 'none');
23 colorbar;
24
25 title('Turbulence Intensity Contour Plot', 'FontSize', 16,
       'FontName', 'Times New Roman');
26 xlabel('X (cm)', 'FontSize', 14, 'FontName', 'Times New
       Roman');
27 ylabel('Y (cm)', 'FontSize', 14, 'FontName', 'Times New
       Roman');
28
29 colormap('parula');
30
31 axis tight;
32
33 pbaspect([52/100, 1, 1]);
34
35 cb = colorbar;
36 cb.FontSize = 14;
37 cb.FontName = 'Times New Roman';
38
39 set(gca, 'FontSize', 14, 'FontName', 'Times New Roman');
```

APPENDIX B: DATA

Detailed Budget Analysis

Table B.1: Detailed Budget Breakdown Used for the Project

S.No	Expense Details	Quantity	Estimated Amount (NPR)	Remarks
		Hardware		
1	Aluminum Rod	4	3,600	900 per unit
2	Bearing	8	400	50 per unit
3	Clear Glass (3.5mm)	2.7 sq.ft	500	185 per sq.ft
4	Coupler	4	1,000	250 per unit
5	Drill Bit (3mm)	10	300	30 per unit
6	Metal Cutting Wheel	4	200	50 per unit
7	Metal Pipe	23 ft	3,450	150 per ft
8	Polycarbon Sheet	5 sq.ft	2,123.85	424.77 per sq.ft
9	Plywood	-	12,000	Flexible + C grade Plywood
10	10mm Nut Bolt	600g	400	700 per kg
		Electronics		
11	3D Printing Machine	1	-	Already available in DMAE Flow Visualization Lab
12	Arduino	1	-	Already available in DMAE Flow Visualization Lab
13	CNC Machining	1	-	Already available in DMAE Flow Visualization Lab
14	Drilling Machine	1	-	Already available in IIEC
15	iPhone 14 Pro Max	1	-	Already available at Team
16	Marble Cutter	-	-	Already available in Robotics Club

17	NEMA 23 Stepper Motors	2	-	Already available in DMAE Flow Visualization Lab
18	Oil Pump	1	2,500	2,500 per unit
19	Pixel 8a	1	-	Already available at Team
20	Plane Laser	1	-	Already available in DMAE Flow Visualization Lab
21	PLA Filament	1	-	Already available in DMAE Flow Visualization Lab
22	Smoke Generator	1	-	Already available in DMAE Flow Visualization Lab
23	Styrofoam	1	-	Already available in DMAE Flow Visualization Lab
24	TB6600 Motor Driver	1	-	Already available in DMAE Flow Visualization Lab
25	Vane Anemometer	1	-	Already available in DMAE Flow Visualization Lab
26	Welding Machine	1	-	Already available in IIEC
Chemical				
27	Black Enamel Paint	1 Ltr	1,000	1,000 per unit
28	Colin	1	113	113 per unit
29	Dendrite	1500 ml	1,225	1,225 per unit
30	Fog Liquid	3 litre	3,000	1000 per litre
31	White Cement	1 kg	70	70 per unit
Miscellaneous				
32	Binding Tape	5	500	100 per unit
33	Black Chart Paper	7	140	20 per unit
34	Electric Tape	2	50	25 per unit

35	Jumper Wires and Connectors	-	100	100 per unit
36	Paint Brush	1	50	50 per unit
37	Double Sided Tape	4	400	100 per unit
38	Nails	5 pkt	450	90 per pkt
Grand Total			**33,571.85**	

Wind Tunnel Data

The velocity recorded by vane anemometer is shown in the Tables[B.2, B.3, B.4]. These values were then averaged to compute the maximum and minimum velocities for obtaining TI.

Table B.2: Recorded Velocity at Grid Data 1 (Outlet)

Maximum					**Minimum**				
7.57	7.87	8.27	8.19	7.72	7.26	7.64	8.14	8.16	7.41
8.00	8.44	8.41	8.19	7.65	7.92	8.27	8.30	8.07	7.47
8.05	8.62	8.60	8.45	8.25	7.87	8.45	8.50	8.37	7.80
7.78	8.76	8.61	8.75	8.66	7.41	8.67	8.36	8.57	8.06
8.04	9.00	9.02	9.01	8.70	7.88	8.92	8.72	8.83	8.52
8.15	8.93	9.10	9.10	8.99	7.79	8.78	8.94	9.00	8.77
7.28	9.07	9.37	9.35	9.26	6.99	8.90	9.01	9.08	9.14
8.24	9.11	9.61	9.58	9.13	8.01	8.92	9.40	9.25	9.05
8.21	9.12	9.66	9.42	9.21	7.82	8.97	9.31	9.02	9.07
7.77	8.90	9.60	9.45	9.00	7.32	8.74	9.38	8.84	8.95

Table B.3: Recorded Velocity at Grid Data 2 (Outlet)

Maximum					**Minimum**				
7.60	7.81	8.40	8.34	7.71	7.45	7.69	8.26	8.12	7.49
8.31	8.46	8.36	8.10	8.03	7.82	8.18	8.12	8.05	7.45
8.02	8.82	8.54	8.25	8.27	7.72	8.64	8.25	8.09	7.74
8.16	8.89	8.68	8.82	8.26	7.55	8.61	8.55	8.36	7.95
7.88	8.73	8.85	9.09	9.01	7.48	8.46	8.61	8.54	8.48
8.15	9.01	9.20	9.20	8.82	7.50	8.33	8.72	8.83	8.73
8.31	9.06	9.22	9.18	9.21	7.77	8.52	8.64	8.86	8.55
8.31	9.20	9.54	9.60	9.30	7.70	9.15	9.04	9.38	8.96
8.20	9.34	9.70	9.45	9.19	7.97	9.11	9.40	9.36	9.10
8.17	9.23	9.80	9.37	9.08	7.85	8.89	9.29	8.87	8.98

Table B.4: Recorded Velocity at Grid Data 3 (Outlet)

Maximum					**Minimum**				
7.77	8.05	8.44	8.25	7.31	7.24	7.76	8.30	7.39	6.20
7.99	8.48	8.45	8.27	7.94	7.94	7.96	8.27	7.39	6.61
8.13	8.73	8.62	8.34	8.43	7.38	8.57	8.21	8.28	7.53
8.22	9.05	8.71	8.59	8.81	7.67	8.60	8.67	8.51	7.73
8.29	9.12	9.15	8.72	8.90	7.72	8.61	8.73	8.65	8.17
8.05	9.24	9.53	9.07	8.95	7.48	8.61	8.93	8.84	8.17
8.02	9.43	9.70	9.58	9.04	7.19	8.86	9.14	9.09	8.27
8.48	9.40	9.85	9.78	9.12	7.02	8.91	9.30	9.32	8.20
8.33	9.50	9.85	9.59	9.19	7.23	9.03	9.51	9.47	8.14
7.99	9.03	9.79	9.39	9.15	6.89	8.93	9.11	8.97	8.19

Table B.5: Averaged Maximum and Minimum Values (Outlet)

Maximum					**Minimum**				
7.65	7.91	8.37	8.26	7.58	7.32	7.70	8.23	7.89	7.03
8.10	8.46	8.41	8.19	7.87	7.89	8.14	8.23	7.84	7.18
8.07	8.72	8.59	8.35	8.32	7.66	8.55	8.32	8.25	7.69
8.05	8.90	8.67	8.72	8.58	7.54	8.63	8.53	8.48	7.91
8.07	8.95	9.01	8.94	8.87	7.69	8.66	8.69	8.67	8.39
8.12	9.06	9.28	9.12	8.92	7.59	8.57	8.86	8.89	8.56
7.87	9.19	9.43	9.37	9.17	7.32	8.76	8.93	9.01	8.65
8.34	9.24	9.67	9.65	9.18	7.58	8.99	9.25	9.32	8.77

Table B.6: Averaged Maximum and Minimum Values (Test Section)

Maximum					**Minimum**				
8.25	8.57	8.95	8.93	8.86	8.06	8.24	8.69	8.85	8.84
8.87	9.10	9.02	8.99	8.85	8.59	8.95	8.93	8.77	8.74
8.41	9.04	9.10	8.97	8.83	8.26	8.87	8.93	8.91	8.75
8.36	8.86	9.14	8.89	8.82	8.00	8.77	8.91	8.82	8.75
8.79	8.77	8.93	8.56	8.79	8.69	8.68	8.71	8.54	8.75
8.60	8.85	8.88	8.78	8.73	8.48	8.69	8.83	8.72	8.63
8.66	8.65	8.76	8.47	8.32	8.50	8.54	8.52	8.30	8.20
8.66	8.66	8.84	8.70	8.73	8.61	8.65	8.69	8.54	8.57
7.88	8.25	8.43	8.45	8.48	7.06	8.15	8.19	8.37	8.23
7.81	8.82	8.25	8.57	7.85	7.68	8.75	8.23	8.45	7.71

Table B.7: Fan Description

Attribute	**CG (6 Fans)**	**Usha (4 Fans)**
Company	CG	Usha
Model	CGFFA030	Farrata EX
Power Rating	130 W	160 W
Motor Speed	1400 rpm	1400 rpm
Number of Fans	6	4
Air Delivery	-	90 m^3/min
Size	20 in	20 in (500 mm)

Mass of Vanes

Table B.8: Mass of the Vane

Chord (cm)	**Mass (g)**
20	140
25	180
30	255

Mass of Spar

Table B.9: Mass of the Aluminum Spar

Diameter (mm)	**Mass (g)**
12	318

Project Timeline

Table B.10: Project Timeline

Task	**Start Date**	**End Date**	**Days**
Literature Review	13-May-24	28-Feb-25	291
Computational & Analytical Work 1st Phase	20-Jun-24	22-Dec-24	185
Development of Actuation System	10-Nov-24	22-Nov-24	12
Development of Gust Generator	22-Nov-24	2-Dec-24	10
Experiment 1st Phase	18-Nov-24	24-Jan-25	67
Flow Visualization	25-Nov-24	1-Mar-25	96
Wind Tunnel Design Optimization	4-Jan-25	12-Jan-25	8
Wind Tunnel Fabrication	15-Jan-25	11-Feb-25	27
Fabrication of New Gust Generator Setup	22-Jan-25	10-Feb-25	19
Experiment 2nd Phase	12-Feb-25	5-Mar-25	21
Computational & Analytical Work 2nd Phase	30-Jan-25	27-Feb-25	28
Data Processing	20-Feb-25	3-Mar-25	11
Documentation	13-May-24	4-Mar-25	295

APPENDIX C: IMAGES

Computational

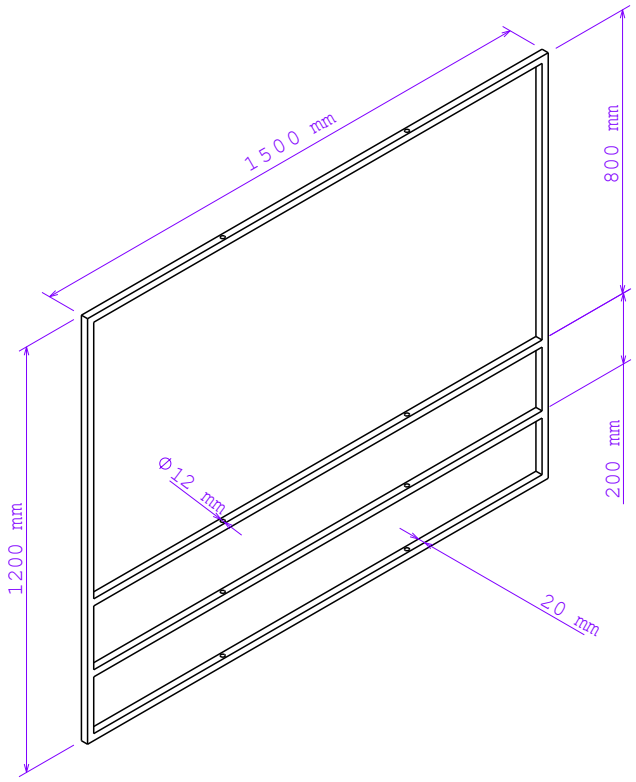

Figure C.1: Initial Frame Design

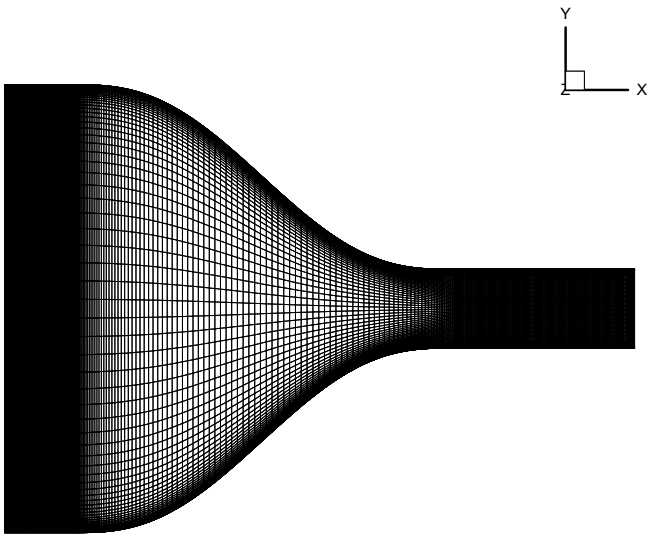

Figure C.2: 2D Mesh for the Wind Tunnel for $2500\ mm$ Contraction Zone Length

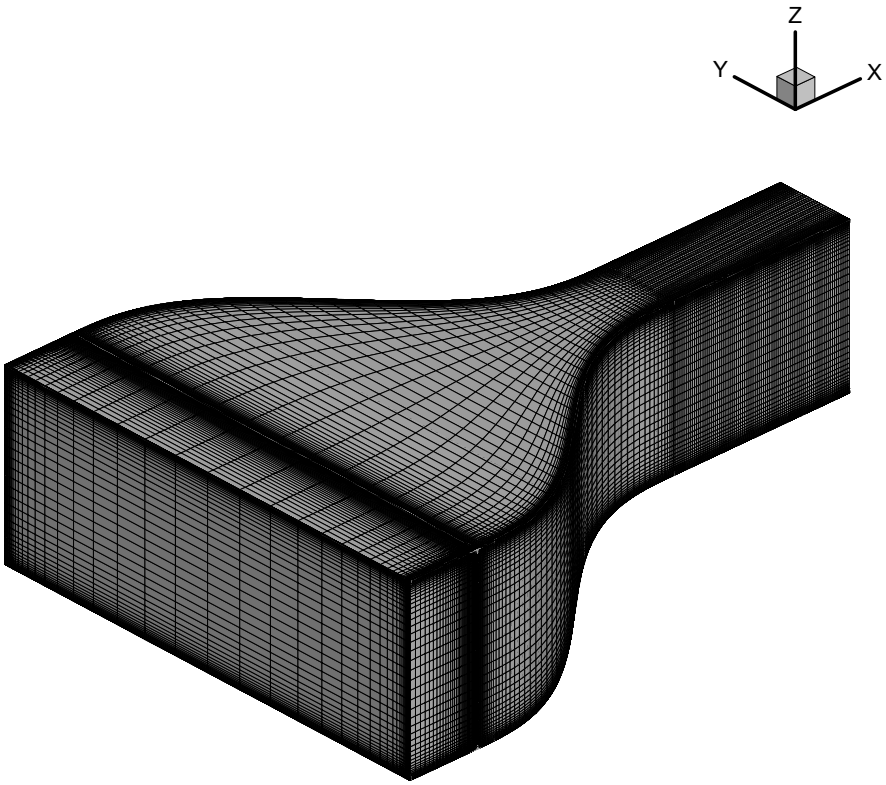

Figure C.3: Medium Mesh of Wind Tunnel

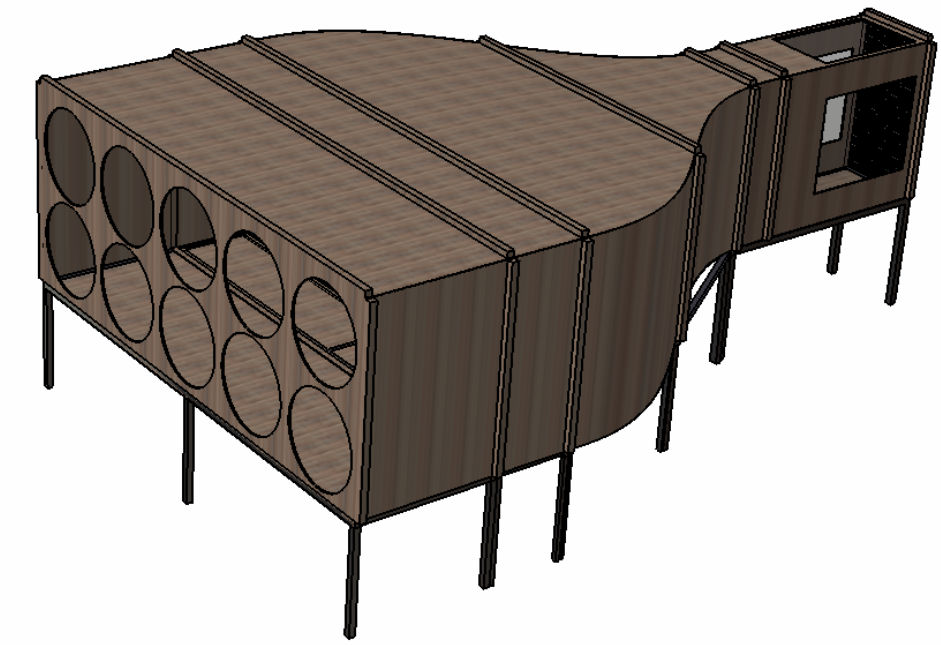

Figure C.4: Assembled Wind Tunnel

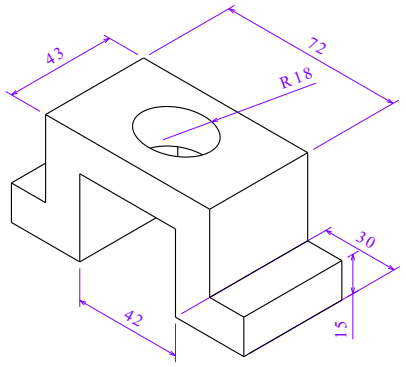

Figure C.5: Housing for Stepper Motor

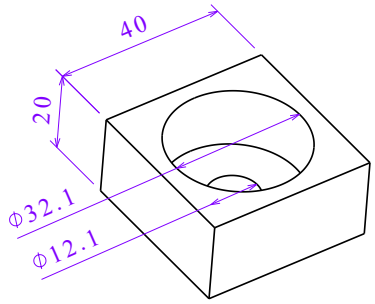

Figure C.6: Housing for 12mm Bearing

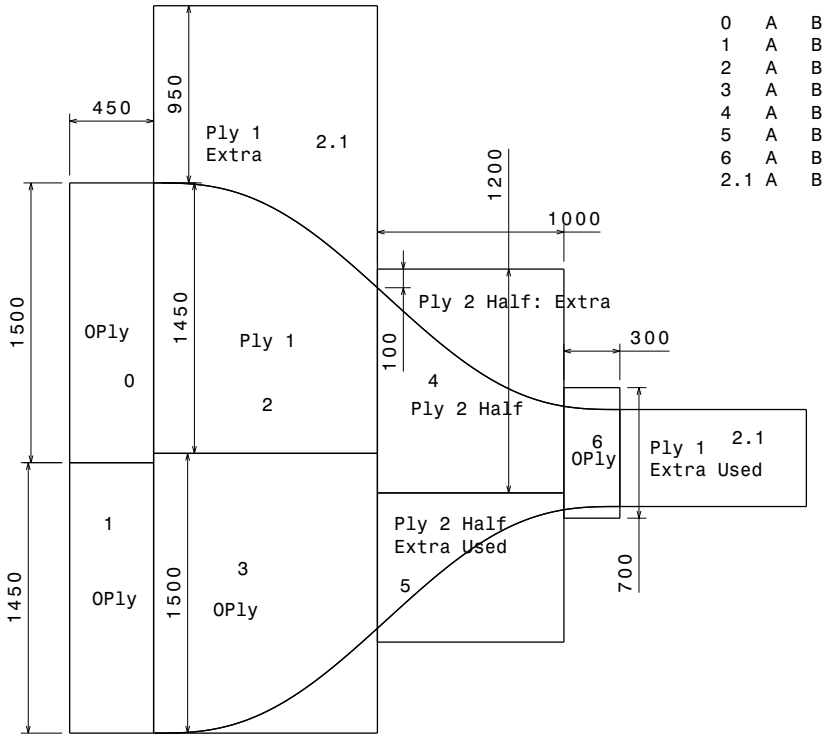

Figure C.7: Plywood Cutting Sections

Fabrication

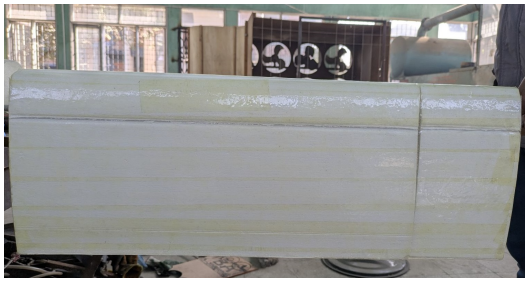

Figure C.8: Fabricated Vane NACA 0016 of $0.25m$ chord

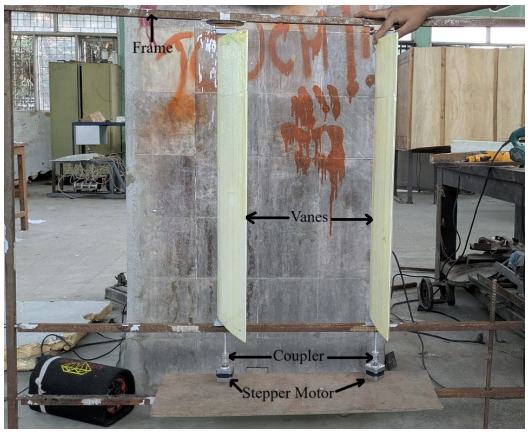

Figure C.9: Integration of Vanes in the Initial Frame

Figure C.10: Assembly of Plywoods for Top View Wind Tunnel

Figure C.11: Assembly of the Tunnel In progress

Figure C.12: Fabricated Wind Tunnel

Figure C.13: Detachable Extension ($520mm(W) \times 1800mm(L) \times 1000mm(H)$)

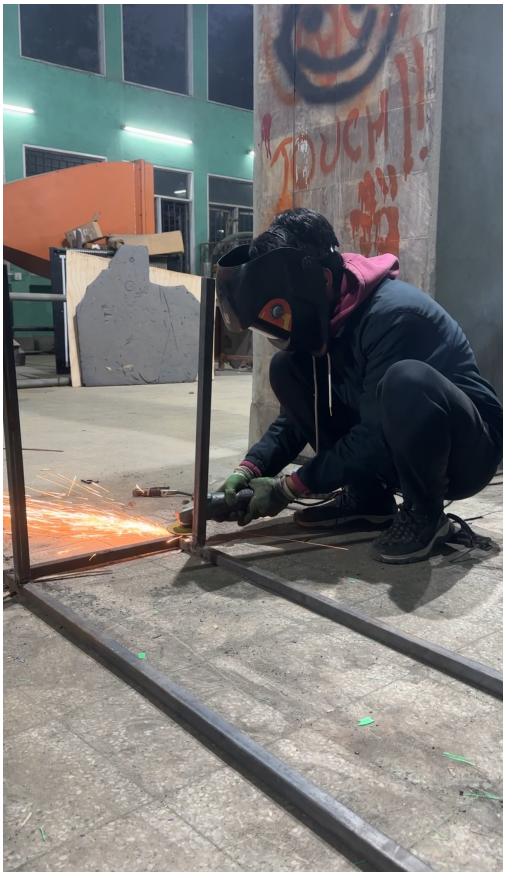

Figure C.14: Frame being Fabricated

Experiment

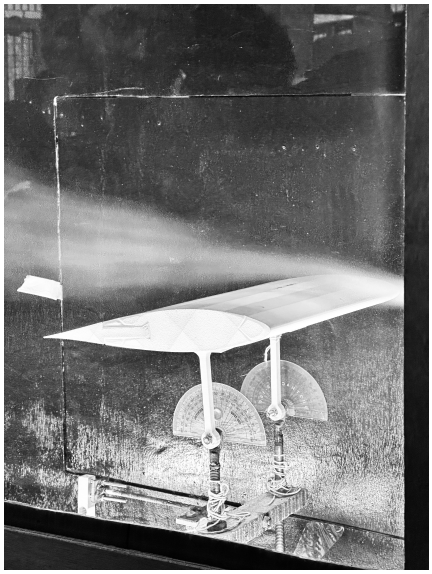

Figure C.15: Smoke Visualization on a Wing Observing Stall Angle

Figure C.16: Rocket Integration in Wind Tunnel with Gust Generator

Figure C.17: Digital Twin Technology being Performed in Wind Tunnel

Figure C.18: Vibration Analysis being done in Wind Tunnel

APPENDIX D: EXPERIMENTAL LOGBOOK

Experiment Details:

- **Objective:** Measure the effects of varying vane spacing (d_h), degree of oscillation (θ), frequency (f), and chord length (c) for producing gust.
- **Vane Details:** Styrofoam.

Variables:

- **Varying Spacing** (dh): 10, 20, 30, 40 cm
- **Varying Degree of Oscillation** (θ): 10, 15, 20, 25 $^\circ$
- **Varying Frequency** (f): 2, 3, 4 Hz
- **Varying Chord Length** (c): 20, 25, 30 cm

Table D.11: Chord Length of $20cm$

Chord Length (c) = 20 cm	
Experiment Number	**Remarks**
1	No effect of the gust was seen at $100\ mm$ spacing, $2\ Hz$, $\theta_{max} = 10^\circ$: Linear Profile Observed
2	There was slight deflection of the flow at $200\ mm$ spacing, $2\ Hz$, $\theta_{max} = 10^\circ$: Linear Profile Observed
3	The profile still remained linear at $200\ mm$ spacing, $3\ Hz$, $\theta_{max} = 10^\circ$: Linear Profile Observed
4	Glimpses of sinusoidal profile was observed at $200\ mm$ spacing, $4\ Hz$, $\theta_{max} = 15^\circ$
5	Glimpses of sinusoidal profile was observed with slight increase in magnitude at at $300\ mm$ spacing, $4\ Hz$, $\theta_{max} = 15^\circ$

Table D.12: Chord Length of $25cm$

Chord Length (c) = 25 cm	
Experiment Number	**Remarks**
1	No Effect of the Gust Response Seen at $200\ mm$ spacing, $2\ Hz$, $\theta_{max} = 10°$: Linear Profile Observed
2	The flow got slightly got deflected at $3\ Hz$, $\theta_{max} = 10°$, $200\ mm$ spacing. The flow was still linear.
3	A weak sinusoidal pattern was observed at $4\ Hz$, $\theta_{max} = 10°$, $200\ mm$ spacing.
4	Glimpses of more desired sinusoidal gust was observed at $4\ Hz$, $\theta_{max} = 15°$, $200\ mm$ spacing.
5	A more pronounced gust was observed at $3Hz$, $\theta_{max} = 15°$, $300\ mm$ spacing
5	An Uniform high magnitude gust was observed at $4Hz$, $\theta_{max} = 15°$, $300\ mm$ spacing

Table D.13: Chord Length of $30cm$

Chord Length (c) = 30 cm	
Experiment Number	**Remarks**
1	Stepper Motor was unable to provide enough torque for the oscillation of the vanes.

11% Overall Similarity

The combined total of all matches, including overlapping sources, for each database.

Filtered from the Report

- Bibliography
- Quoted Text
- Cited Text
- Small Matches (less than 8 words)

Match Groups

99 Not Cited or Quoted 11%
Matches with neither in-text citation nor quotation marks

0 Missing Quotations 0%
Matches that are still very similar to source material

0 Missing Citation 0%
Matches that have quotation marks, but no in-text citation

0 Cited and Quoted 0%
Matches with in-text citation present, but no quotation marks

Top Sources

9% Internet sources
7% Publications
0% Submitted works (Student Papers)

Integrity Flags

2 Integrity Flags for Review

Replaced Characters
23 suspect characters on 14 pages
Letters are swapped with similar characters from another alphabet.

Hidden Text
218 suspect characters on 5 pages
Text is altered to blend into the white background of the document.

Our system's algorithms look deeply at a document for any inconsistencies that would set it apart from a normal submission. If we notice something strange, we flag it for you to review.

A Flag is not necessarily an indicator of a problem. However, we'd recommend you focus your attention there for further review.

Match Groups

- **99** Not Cited or Quoted 11%
  Matches with neither in-text citation nor quotation marks
- **0** Missing Quotations 0%
  Matches that are still very similar to source material
- **0** Missing Citation 0%
  Matches that have quotation marks, but no in-text citation
- **0** Cited and Quoted 0%
  Matches with in-text citation present, but no quotation marks

Top Sources

- 9% Internet sources
- 7% Publications
- 0% Submitted works (Student Papers)

Top Sources

The sources with the highest number of matches within the submission. Overlapping sources will not be displayed.

1	Internet	
par.nsf.gov		<1%
2	Internet	
dokumen.pub		<1%
3	Internet	
www.mdpi.com		<1%
4	Publication	
Kieran T. Wood, Ronald C. Cheung, Thomas S. Richardson, Jonathan E. Cooper, Oli...		<1%
5	Publication	
Anya R. Jones, Oksan Cetiner, Marilyn J. Smith. "Physics and Modeling of Large Flo...		<1%
6	Publication	
Yığılı, İmge. "Design and Experimental Investigation of a Wind Tunnel Gust Gener...		<1%
7	Internet	
dspace.houghton.edu		<1%
8	Internet	
www.grin.com		<1%
9	Internet	
www.yumpu.com		<1%
10	Publication	
Ethirajan Rathakrishnan. "Instrumentation, Measurements, and Experiments in F...		<1%

11 Publication
Iacopo Carnacina, Mawada Abdellatif, Manolia Andredaki, James Cooper, Darren ... <1%

12 Internet
su2foundation.org <1%

13 Internet
casopisi.junis.ni.ac.rs <1%

14 Publication
Hari Sharan Dangi, Dipendra Basnet, Roman Shrestha, Utsav Karki. "Design, Cons... <1%

15 Internet
archive.org <1%

16 Internet
ntrs.nasa.gov <1%

17 Internet
entri.app <1%

18 Internet
theses.gla.ac.uk <1%

19 Publication
Folan, . "ELECTRICITY AND MAGNETISM", Modern Physics And Technology For Un... <1%

20 Publication
Haigang Tian, Tianyi Hao, Chao Liu, Han Cao, Xiaobiao Shan. "Investigation of a P... <1%

21 Internet
www.mhtlab.uwaterloo.ca <1%

22 Publication
Henryk Anglart. "Multilingual Dictionary of Nuclear Reactor Physics and E... <1%

23 Publication
Messina, M.. "Experimental validation of pressure loss in anemometer testing eq... <1%

24 Publication
Andrei D. Polyanin, Alexander V. Manzhirov. "Handbook of Mathematics for Engin... <1%

25 Publication
Dilek Funda Kurtulus. "On the wake pattern of symmetric airfoils for different inc... <1%

26 Publication
Ravi P. Agarwal, Donal O'Regan. "Chapter 9 Bessel Functions", Springer Science a... <1%

27 Internet
data.nanet.go.kr <1%

28 Internet
ijera.com <1%

29 Internet
pdfcoffee.com <1%

30 Internet
www.dicat.unige.it <1%

31 Publication
Gower, Blake Ernest. "Aerodynamic Design and Characterization of Novel Wound ... <1%

32 Publication
Yordan Garbatov, C. Guedes Soares. "Innovation in the Analysis and Design of Ma... <1%

33 Internet
esth.koha-ptfs.co.uk <1%

34 Publication
Anya R. Jones, Oksan Cetiner, Marilyn J. Smith. "Physics and Modeling of Large Flo... <1%

35 Publication
Zhenlong Wu. "Rotor power performance and flow physics in lateral sinusoidal g... <1%

36 Internet
ir.busitema.ac.ug <1%

37 Internet
eprints.soton.ac.uk <1%

38 Internet
www.mhtl.uwaterloo.ca <1%

39 Internet
dergipark.org.tr <1%

40 Internet
forex-trading-courses.com <1%

41 Publication
Wim Van Hoydonck, Michael Van Tooren, Marc Gerritsma. "Vortex Filament Simul... <1%

42 Internet
deepblue.lib.umich.edu <1%

43 Internet
instrepo-prod.cc.uregina.ca <1%

44 Internet
theses-test.ncl.ac.uk <1%

45 Internet
www.projectreserve.com <1%

46 Internet
www.seas.upenn.edu <1%

47 Internet
www.solid.lth.se <1%

48 Publication
Chandrakant S. Desai, Musharraf Zaman. "Advanced Geotechnical Engineering - S... <1%

49 Publication
Poudel, Naresh. "Aerodynamic Analysis of Stationary and Flapping Wings in Unst... <1%

50 Publication
Sencan, Gizem. "Effect of Wing Heating on Flow Structure of Low Swept Delta Win... <1%

51 Publication
Thiago de Souza Siqueira Versiani, Flávio J. Silvestre, Antônio B. Guimarães Neto, ... <1%

52 Internet
digitalcommons.library.umaine.edu <1%

53 Internet
openaccess.city.ac.uk <1%

54 Internet
pastel.archives-ouvertes.fr <1%

55 Internet
res.mdpi.com <1%

56 Internet
unsworks.unsw.edu.au <1%

57 Internet
worldwidescience.org <1%

58 Internet
www.research-collection.ethz.ch <1%

59 Internet
www.scribd.com <1%